BAR-ILAN UNIVERSITY

Second Harmonic Generation and Pulse Characterization of Ultrashort X-Ray Pulses

Shimon Yudovich

Submitted in partial fulfillment of the requirements for the Master's Degree in the Department of Physics, Bar-Ilan University

Ramat Gan, Israel 2015

This work was carried out under the supervision of

Dr. Sharon Shwartz

Department of Physics, Bar-Ilan University

Acknowledgement

I would like to express my sincere gratitude to Dr. Sharon Shwartz for guiding, teaching and supporting me throughout my MSc work.

I would like to thank my teachers and lecturers throughout the years, who encouraged and motivated me to study and explore nature.

I also thank the Physics Department administrative staff at Bar-Ilan University for the practical support during my undergraduate and MSc studies.

Finally, I would like to thank my family and friends for supporting me through all these years.

Contents

Abstract

The successful operation of x-ray free electron lasers (XFELs), producing highly brilliant ultrashort x-ray pulses, has introduced a new invaluable tool for the science of light-matter interactions. These new 'fourth-generation synchrotrons' were recently used in order to study nonlinear optical processes, expanding the field of nonlinear optics to the x-ray regime. In this work, I theoretically study two topics regarding nonlinear optics at x-ray wavelengths, and consider its differences from the more studied optical regime.

The first topic I examine is the process of x-ray second harmonic generation (SHG) from focused ultrashort pulses. The propagation geometry of this process results in two distinct features. First, it highly limits the overlap length between the pump beam and the generated second harmonic (SH). Second, the generated SH is partially Bragg scattered. In this work, I concentrate on the usage of focused ultrashort pump pulses, which are crucial for observing this weak nonlinear effect. In order to study different aspects of this process and its optimization, I numerically simulate and derive approximated analytical expressions for the efficiency and tolerances of the SHG process.

The second topic of this work is a method for measuring the temporal field profile of ultrashort x-ray pulses including phase information. Based on a successful characterization method at the optical regime, the scheme relies on the spectral interference pattern of two replicas of the same pulse, which are spectrally shifted via nonlinear three-wave mixing with IR or visible beams. Using a single-shot spectrometer the scheme can inspect, for the first time, individual ultrashort x-ray pulses with random amplitudes and phases. Examples for characterization of stochastic pulses are given, including criteria for a successful measurement.

1. Introduction

Light-matter interaction may be seen as coupling between Maxwell's equations (governing the electromagnetic field) and, in case of classical particles, Newton's equation (governing the motion of electrical charge). This coupling explains how the electromagnetic field induces time-varying polarization in the material, and this, in return, radiates and acts as a source for the electromagnetic field.

We start by introducing three important concepts for the following discussion of nonlinear processes at hard x-rays – the models for the linear and nonlinear induced currents, and the wave propagation equations.

1.1. Linear Interaction in Periodic Structures

The basis of linear optics is the linear dependence of the material polarization on the incoming field, $P_i = \varepsilon_0 \chi_{ij}^{(1)} E_j$, where the Einstein summation convention is applied, i and j represent Cartesian components, ε_0 is the vacuum permittivity, and $\chi_{ij}^{(1)}$ is the linear electric susceptibility tensor.

In the hard x-ray regime, high above resonances, the linear interaction is described by Thomson scattering [1], giving the susceptibility $\chi(\vec{r}) = -\frac{R\lambda^2 \rho(\vec{r})}{\pi}$, where $\rho(\vec{r})$ is the charge distribution, λ is the wavelength of the driving field, and $R = \frac{q^2}{4\pi\varepsilon_0 m_e c^2}$ is the classical radius of the electron, with m_e and q being the electron mass and charge, respectively. Since the electron charge distribution in ordered crystals is

periodic, we may expand $\rho(\vec{r})$ in a Fourier series $\rho(\vec{r}) = \sum_m \rho_m e^{i\vec{G}_m \cdot \vec{r}}$, where $\rho_m = \frac{1}{V}\int_V \rho(\vec{r}) e^{-i\vec{G}_m \cdot \vec{r}} dv$ is its Fourier components, with $\vec{\mathrm{G}}_m$ being the reciprocal vectors and with the integration carried over the unit cell volume V. Similarly, we perform a Fourier expansion of $\chi(\vec{r})$:

$$\chi_m = -\frac{R\lambda^2 \rho_m}{\pi}. \tag{1.1}$$

χ_m is the coupling coefficient for the elastic Bragg scattering process, where $\vec{\mathrm{G}}_m$ is the transferred momentum between the incoming and outgoing waves. χ_0 contributes to the usual forward propagation of the wave (which defines the index of refraction $n = \sqrt{1+\chi_0}$).

1.2. Nonlinear Interactions

For sufficiently intense electromagnetic fields, the induced polarization dependence upon the field is no longer linear. Consequently, the nonlinear response may be presented by generalizing the linear dependence introduced last section with higher order terms $P_i = \varepsilon_0\left[\chi_{ij}^{(1)} E_j + \chi_{ijk}^{(2)} E_j E_k + \chi_{ijkl}^{(3)} E_j E_k E_l + \ldots\right]$. Nonlinear optics, which is the study and application of the nonlinear response of matter to light, developed shortly after the operation of the first working laser by Maiman in 1960. The high intensity of lasers has been used in order to observe and utilize this nonlinear response in various ways, such as generating light in new frequencies, and optically manipulating the phase and amplitude of light. In addition, nonlinear effects have been observed for various materials and states of matter, including liquids, gas

vapors and plasma. The nature and magnitude of the nonlinear optical susceptibility depends both on the structure and arrangement of the nonlinear medium, and on the frequencies participating in the nonlinear process.

Since non-resonant nonlinearities decrease with frequency, and since high-brilliant sources in the x-ray portion of the electromagnetic spectrum have been absent until very recently, nonlinear phenomena, such as second harmonic generation (SHG), have not been reported in this regime. Indeed, with earlier hard x-ray sources – x-ray tubes and third generation synchrotrons, only spontaneous parametric down conversion (SPDC) has been observed [2-4]. This process relies on the vacuum field as one of the driving fields for the nonlinear interaction, and the large density of states of electromagnetic modes at x-ray wavelengths compensates for the low nonlinear coupling. The construction of hard x-ray free electron lasers (XFELs), producing femtosecond pulses of high brightness and peak intensity, led to the possibility of preforming farther experiments exploring nonlinear effects at x-ray wavelengths.

In order to describe the nonlinear interaction at the x-ray regime, we consider a classical model of cold collisionless plasma fluid, as proposed by Eisenberger et al. [2]. First we write the equations of motion and continuity [5]:

$$\frac{\partial \vec{v}}{\partial t} + \vec{v} \cdot \nabla \vec{v} = -{\omega_b}^2 x + \frac{\lambda q}{m_e}\left(\vec{E} + \vec{v} \times \vec{B}\right), \tag{1.2a}$$

$$\frac{\partial \rho}{\partial t} + \nabla \cdot \left(\rho \vec{v}\right) = 0. \tag{1.2b}$$

Where $\vec{v}(\vec{r},t)$ is the velocity field of electrons, $\rho(\vec{r},t)$ is the electron density and $\hbar\omega_b$ is the dominant electron binding energy. The nonlinear current $\vec{J}_{NL}$ is obtained by using a perturbative approach. With λ being a small perturbation parameter, we expand both the velocity and the electron density up to second order $\vec{v} \approx \lambda\vec{v}^{(1)} + \lambda^2\vec{v}^{(2)}$, $\rho \approx \rho^{(0)} + \lambda\rho^{(1)} + \lambda^2\rho^{(2)}$. Setting $\lambda = 1$, the second order nonlinear current $\vec{J}_{NL} = \rho^{(0)}\vec{v}^{(2)} + \rho^{(1)}\vec{v}^{(1)}$ for a general three-wave mixing process of $\frac{1}{2}E_1 e^{i\left(\vec{k}_1\cdot\vec{r}-\omega_1 t\right)}\hat{e}_1 + c.c$ and $\frac{1}{2}E_2 e^{i\left(\vec{k}_2\cdot\vec{r}-\omega_2 t\right)}\hat{e}_2 + c.c$ is therefore:

$$\vec{J}_{NL} = -\frac{q^2\rho_G E_1 E_2}{4m_e^2}\left[\vec{A}_{Doppler} + \vec{A}_{disp} + \vec{A}_{Lorentz}\right]e^{i\left(\vec{k}_1+\vec{k}_2+\vec{G}\right)\cdot\vec{r}-i(\omega_1+\omega_2)t} + c.c. \qquad (1.3)$$

We define $\beta_i = \frac{q\rho_0}{m\left(\omega_i^2 - \omega_b^2\right)\varepsilon_0}$ for $i = 1,2$, and choose to phase-match the process with a specific reciprocal vector $\vec{G}$. Following Eisenberger et al. [2], we identify three mechanisms contributing to the nonlinear response:

(i) The Doppler current:

$$\vec{A}_{Doppler} = \frac{\omega_2\left(\vec{G}\cdot\hat{e}_1\right)\hat{e}_2}{\left(1-\beta_1\right)\left(\omega_1^2-\omega_b^2\right)\left(\omega_2^2-\omega_b^2\right)} + \frac{\omega_1\left(\vec{G}\cdot\hat{e}_2\right)\hat{e}_1}{\left(1-\beta_2\right)\left(\omega_1^2-\omega_b^2\right)\left(\omega_2^2-\omega_b^2\right)}, \qquad (1.4a)$$

arising from the inelastic scattering of one field by the charge oscillating as a result of the other field.

(ii) The displacement current:

$$\vec{A}_{disp} = \frac{\left(\omega_1+\omega_2\right)}{\left[\left(\omega_1+\omega_2\right)^2-\omega_b^2\right]}\left[\frac{\omega_1\omega_2}{\left(\omega_1^2-\omega_b^2\right)\left(\omega_2^2-\omega_b^2\right)}\left[\left(\hat{e}_1\cdot\vec{k}_2\right)\hat{e}_2 + \left(\hat{e}_2\cdot\vec{k}_1\right)\hat{e}_1\right]\right], \qquad (1.4b)$$

arising from the scattering of one field while it is displaced by the other field.

(iii) The nonlinear Lorentz current:

$$\vec{A}_{Lorentz} = \frac{\left(\omega_1 + \omega_2\right)}{\left[\left(\omega_1 + \omega_2\right)^2 - {\omega_b}^2\right]}\left[\frac{\omega_1}{\left({\omega_1}^2 - {\omega_b}^2\right)\omega_2}\hat{e}_1 \times \left(\vec{k}_2 \times \hat{e}_2\right) + \frac{\omega_2}{\left({\omega_2}^2 - {\omega_b}^2\right)\omega_1}\hat{e}_2 \times \left(\vec{k}_1 \times \hat{e}_1\right)\right], \tag{1.4c}$$

arising from the Lorentz force where the charge velocity originates from one field and the applied magnetic field from the other field.

We note that unlike conventional nonlinear optics at the optical regime, where second order nonlinearities vanish for centrosymmetric media, the short wavelength of x-rays results in a local space-dependent optical response. Due to this spatial inhomogeneity, second order nonlinear effects may be observed using centrosymmetric media.

1.3. The wave equations

In this section I wish to concentrate on the process of SHG and to introduce the wave equations that will be used in the following discussion.

An efficient SHG occurs when the SH fields generated in different regions of the nonlinear medium interfere constructively. This is known in nonlinear optics as phase-matching (Fig. 1.1), and its mathematical description will be presented later in this section.

Since the indices of refraction at both the pump and the SH frequencies are close, the perfect phase-matching angles of the pump beam and the generated SH will be

close to satisfying the Bragg condition for the SH frequency. For this reason, as pointed up by Nazarkin et al. [6], it may be important to take into considerations the coupling between the nonlinearly generated SH mode and its elastically scattered mode.

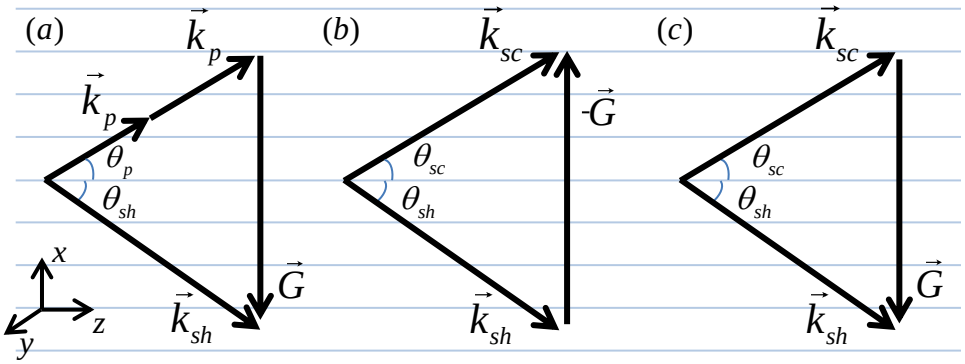

FIG. 1.1. Three phase-matching schemes. ***(a)*** *SHG,* ***(b)*** *scattered SH and* ***(c)*** *back-scattered SH.*

We now describe the propagation equations for the envelopes of the nonlinearly generated SH field E_{sh} and its elastically scattered field E_{scat}. We simplify the wave equation, which is derived from Maxwell's equations, by separating the electric fields as $\tilde{E}_i(\vec{r},t)=\frac{1}{2}E_i(\vec{r},t)e^{i\vec{k}_i\cdot\vec{r}-2i\omega t}\hat{e}_i+c.c.$ where $E_i(\vec{r},t)$ is the envelope function over the $e^{i\vec{k}_i\cdot\vec{r}-2i\omega t}$ carrier wave. Assuming the optical axis is along z_i, we take the slowly varying envelope approximation (SVEA) [7], i.e. $\left|\frac{\partial^2 E_i}{\partial z_i^2}\right|\ll\left|k_i\frac{\partial E_i}{\partial z_i}\right|$, $\left|\frac{\partial^2 E_i}{\partial t^2}\right|\ll\left|\omega\frac{\partial E_i}{\partial t}\right|$, for both modes, which assumes that the envelope changes slowly compared to the carrier wave. Also, we assume an undepleted pump, which is valid because of the low efficiency of this process.

By using these approximations, we write the equations governing the electric field envelopes of the two SH modes:

$$\frac{\partial E_{sh}}{\partial z'}-\frac{i}{2k(2\omega_0)}\left(\frac{\partial^2 E_{sh}}{\partial x'^2}+\frac{\partial^2 E_{sh}}{\partial y^2}\right)+\frac{1}{v_g(2\omega_0)}\frac{\partial E_{sh}}{\partial t}= \\ \frac{q^2\rho_G E_1 E_2}{4m_e^2}\eta(2\omega_0)\left[\left(\vec{A}_{Doppler}+\vec{A}_{disp}+\vec{A}_{Lorentz}\right)\cdot\hat{e}_{sh}\right]e^{i\Delta\vec{k}_{NL}\cdot\vec{r}} \\ +i\varepsilon_0\eta(2\omega_0)\left[\hat{e}_{scat}\cdot\hat{e}_{sh}\right]\omega_0\chi_G E_{scat}e^{i\Delta\vec{k}_B\cdot\vec{r}}, \tag{1.5a}$$

$$\frac{\partial E_{scat}}{\partial \tilde{z}}-\frac{i}{2k(2\omega_0)}\left(\frac{\partial^2 E_{scat}}{\partial \tilde{x}^2}+\frac{\partial^2 E_{scat}}{\partial y^2}\right)+\frac{1}{v_g(2\omega_0)}\frac{\partial E_{scat}}{\partial t}= \\ i\varepsilon_0\eta(2\omega_0)\left[\hat{e}_{sh}\cdot\hat{e}_{scat}\right]\omega_0\chi_{-G}E_{sh}e^{-i\Delta\vec{k}_B\cdot\vec{r}}. \tag{1.5b}$$

Where z' and $\tilde{z}$ are the axes along the propagation directions of the generated SH and its elastically scattered mode, respectively. Similarly, x' and $\tilde{x}$ are the axes normal to the propagation directions of both beams. We assume negligible absorption of the SH field. $\Delta\vec{k}_{NL}=2\vec{k}_p+\vec{G}-\vec{k}_{sh}$ and $\Delta\vec{k}_B=\vec{k}_{sc}+\vec{G}-\vec{k}_{sh}$ are the phase mismatch vectors for the nonlinear and Bragg scattering processes, respectively. k and η are the wave vector and impedance inside the material, respectively, ω_0 is the pump frequency, v_g is the group velocity, and χ_G is the $\vec{G}$ Fourier component of the linear susceptibility.

1.4. Numerical Approach for Solving the Wave Equations

In order to numerically solve Eqs. (1.5) in the following chapters, we turn the partial differential equations into ordinary differential equations (ODEs) by performing a fast-Fourier-transform with respect to time and the spatial coordinates parallel to the boundary surface. Next, we integrate the ODEs with respect to the spatial

coordinate normal to the boundary surface over the crystal length. The integrations are performed using high-order Runge-Kutta and finite difference methods. Since the remaining derivatives in the ODEs are with respect to the coordinate normal to the surface, boundary conditions are easily considered.

2. Second Harmonic Generation of Focused Ultrashort X-Ray Pulses

SHG was the first nonlinear optical effect observed following the demonstration of the first working laser [8]. However, in the absence of a sufficiently intense x-ray source, SHG at x-ray wavelengths was not observed until recently, with the construction of the first operating XFELs. Using the SPring-8 Angstrom Compact free electron laser (SACLA), Shwartz et al. [9] observed SHG from pump pulses at 7.3 keV with an average intensity of ~10^{16} W/cm^2, measuring a maximal conversion efficiency of 1.2×10^{-10}. This measurement confirmed with expected properties of this process such as phase-matching angles and the quadratic scaling of the second harmonic (SH) counts with the pulse energy.

As mentioned in section 1.3, Nazarkin et al. [6] considered in their theoretical study of x-ray SHG in perfect crystals the coupling between the generated SH and its elastically scattered wave in the quasi-monochromatic and plane-wave regime. In their paper, a condition for an optimal synchronous propagation of the two SH fields was presented, which depended on both the linear and nonlinear susceptibilities. However, with the present XFELs obtainable brightness and pulse-energies, and because of the low second order nonlinear coupling of this process, it is necessary to use focused and short pulses in order to achieve high efficiency for a given pulse energy. Here I expand the model suggested by Nazarkin et al. for pump pulses which are finite in time and space.

The goal of this work is thus to study the process of x-ray SHG from short and focused pump beams, propagating in a perfect crystal, generating a SH signal which, in turn, also propagates inside the crystal. Focusing in the spatial and temporal domains increases the peak intensity, giving higher efficiency; however, focusing too tight may decrease the SHG efficiency due to diffraction (when the process occurs over a length longer than the Rayleigh length) and spatial and temporal walk-off between the pump beam and the generated SH.

Using different models of the pump pulse inducing the nonlinear current inside the crystal, I solve the relevant envelope wave equations for the generated SH signal. The purpose of this work is to simulate in detail the recent performed SHG measurement by Shwartz et al. [9], and discuss different aspects of the SH signal propagation, dependence upon the different parameters, and its efficiency optimization.

2.1. Second Harmonic Generation at X-Ray Wavelengths

Assuming a classical model of cold collisionless plasma fluid for the induced nonlinear current, as in Ch. 1, and a pump frequency ω_0 which is much higher than any bound electronic state in the material, we use Eq. (1.3) in order to find the nonlinear current density which drives the SH field for a specific reciprocal vector $\vec{G}$. Since we assume the nonlinear current density is induced by a single pump beam, Eq. 1.4b identically vanishes. Hence, only the Doppler (Eq. 1.4a) and Lorentz (Eq. 1.4c) terms contribute to the nonlinear response.

Using a pump field in the form of $\tilde{E}_p(\vec{r},t)=\frac{1}{2}E_p(\vec{r},t)e^{i\vec{k}_p\cdot\vec{r}-i\omega_0 t}\hat{e}_p+c.c.$, we write the induced nonlinear current density [6]:

$$\vec{J}_{NL}\cdot\hat{e}_{sh}=\frac{1}{2}\left\{-\frac{q^2\rho_G {E_p}^2}{4{m_e}^2{\omega_0}^3}\left[\vec{k}_p+2\left(\vec{G}\cdot\hat{e}_p\right)\hat{e}_p\right]\cdot\hat{e}_{sh}\right\}e^{i\left(\left(2\vec{k}_p+\vec{G}\right)\cdot\vec{r}-2\omega_0 t\right)}+c.c. \qquad (2.1)$$

With $\hat{e}_p$ and $\hat{e}_{sh}$ being the pump and SH field polarization vectors, respectively.

Furthermore, we can use Eq. (2.1) in order to write the second order nonlinear susceptibility $\chi^{(2)}(2\omega_0;\omega_0,\omega_0)=-\frac{iq^2\rho_G}{4\varepsilon_0{m_e}^2{\omega_0}^4}\left[\vec{k}_p+2\left(\vec{G}\cdot\hat{e}_p\right)\hat{e}_p\right]\cdot\hat{e}_{sh}$.

Taking the pump to be polarized in the scattering plane (π-polarization), and assuming the phase-matching angles for both the pump and SH signal are close to the Bragg angle of the SH frequency $\theta_p,\theta_{sh}\approx\theta_B$, we may write Eq. (2.1) as [6]:

$$\vec{J}_{NL}\cdot\hat{e}_{sh}=-\frac{q^2\rho_G {E_0}^2 G\cos(\theta_B)}{16{m_e}^2{\omega_0}^3}\left[1-4\cos(2\theta_B)\right]e^{i\left(\left(2\vec{k}+\vec{G}\right)\cdot\vec{r}-2\omega_0 t\right)}+c.c., \qquad (2.2)$$

or $\chi^{(2)}(2\omega_0;\omega_0,\omega_0)=-\frac{iq^2\rho_G G\cos(\theta_B)}{8\varepsilon_0{m_e}^2{\omega_0}^4}\left[1-4\cos(2\theta_B)\right]$.

We note that in a uniform plasma (where only the ρ_0 component of the charge density is nonzero), the nonlinear current oscillates in the direction of the pump beam propagation. Since there is no component of the nonlinear current density which is transverse to this direction, the generated SH wave vanishes at the far-field. For this reason, a medium with periodic charge distribution (a perfect crystal) is used

as the nonlinear medium. In such media, a wave propagating in a direction satisfying the Bragg condition scatters elastically by the known Bragg diffraction process.

In addition, it is also important to note that we consider the regime in which on the one hand, the pump frequency is much higher than any resonance frequency in the system, so all of the electrons in an atom react the same and constitute the cold plasma. On the other hand, the photon energy is much less than the electron rest energy, so relativistic dynamics are neglected.

As mentioned in the previous chapter, since the phase-matched angle for the SH wave is close to its Bragg angle, a fraction of the generated SH may be elastically diffracted. To consider this effect, we take into account two SH modes when writing the envelope wave equations (Eqs. 1.5): The first one being generated from the SHG process E_{sh}, and the second one being its Bragg scattered wave E_{scat}, as shown in Fig. 1.1.

2.2. Modeling the X-Ray Free Electron Laser Pump Pulse

I start the investigation of our problem by describing models for the input pump pulse structure. First, we write the general complex amplitude of a linearly chirped Gaussian pulse [10]:

$$E_p\left(x_p, y, z_p, t\right) = \frac{E_0 \exp\left(-\alpha_p z_p\right)}{\sqrt{\left(1-i\tau_x\left(z_p\right)\right)\left(1-i\tau_y\left(z_p\right)\right)}} \times \exp\left(-\frac{x_p^2}{w_{0,x}^2\left(1-i\tau_x\left(z_p\right)\right)} - \frac{y^2}{w_{0,y}^2\left(1-i\tau_y\left(z_p\right)\right)} - \frac{\left(1+i\zeta\right)}{\tau^2}\left(t-\frac{z_p}{v_g\left(\omega_0\right)}\right)^2\right). \quad (2.3)$$

Where $\tau_x = \frac{2\left(z_p - z_{0,x}\right)}{b_x}$ and $\tau_y = \frac{2\left(z_p - z_{0,y}\right)}{b_y}$, z_p is the propagation axis of the pump pulse and x_p is the orthogonal axis parallel to the scattering plane. α_p is the field absorption coefficient. $w_{0,x}$, $w_{0,y}$ and τ determine the Gaussian pulse size and duration, respectively. $z_{0,x}$ and $z_{0,y}$ set the focal points, ζ defines the linear chirp and $b_x = k\left(\omega_0\right)w_{0,x}^2$, $b_y = k\left(\omega_0\right)w_{0,y}^2$ are the confocal parameters inside the material.

The input pump pulse is modeled in three ways, all having the same Gaussian power spectrum with full width at half maximum (FWHM) bandwidth ΔE: (a) transform limited (TL) Gaussian pulse, i.e. $\zeta = 0$ – having the minimal pulse duration $\tau_0 = \frac{2\sqrt{2\ln 2}\hbar}{\Delta E}$ ($\hbar$ being the reduced Planck's constant), (b) linearly chirped pulse (LC) – having the estimated pulse duration τ by taking the linear chirp coefficient as $\zeta = \sqrt{\frac{\Delta E^2\tau^2}{8\hbar^2\ln 2} - 1}$, and (c) temporally-stochastic x-ray pulses – a closely-packed and equally spaced train of coherent Gaussian spikes with random phases, as the following:

$$E\left(z_p, t\right) = \exp\left[-\frac{1}{\tau^2}\left(t - \frac{z_p}{v_g\left(2\omega_0\right)}\right)^2\right]\sum_{m=-\infty}^{\infty}\exp\left[i\xi_m\right]\exp\left[-\frac{1}{\tau_0^2}\left(t - m\cdot\Delta\tau - \frac{z_p}{v_g\left(2\omega_0\right)}\right)^2\right]. \tag{2.4}$$

Here $\Delta\tau$ is the duration between the spikes (taken to be $\Delta\tau = \frac{\tau_0}{5}$). Practically, the summation index m takes enough values so that the constituting spikes cover the Gaussian envelope. For each pulse we generate a set $\left\{\xi_m\right\}$ of uniformly distributed

$[0, 2\pi]$ random numbers. Similar to Ref. [11], the average over a large number of these stochastic pulses corresponds to an assumed average Gaussian pulse structure of duration τ (see Fig. 2.1).

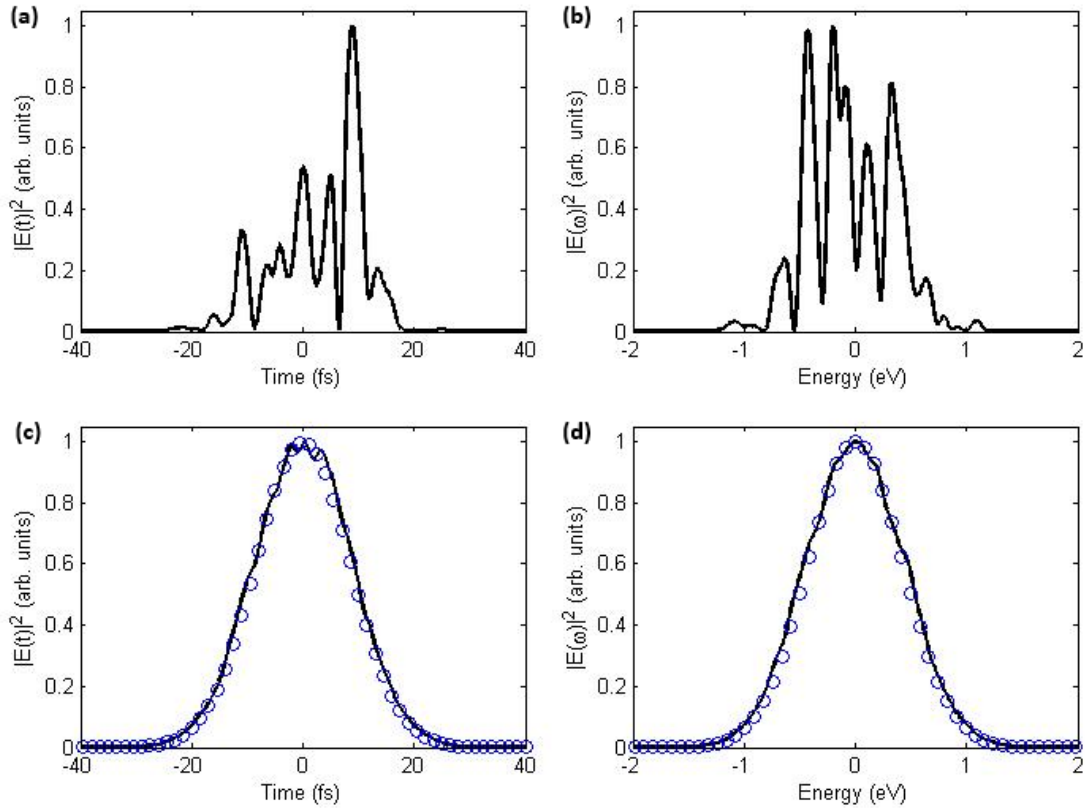

FIG. 2.1. The input pump pulse. ***(a)*** *and* ***(b)*** *show the intensity and power spectrum, respectively, of a single stochastic pulse realization, assuming an average FWHM bandwidth of 1 eV and an average FWHM duration of 20 fs. The spectrum is shown as a function of the photon energy relative to the central energy.* ***(c)*** *and* ***(d)*** *show the averaged intensity and power spectrum, respectively, over 1000 stochastic pulse realizations (black solid lines), plotted along the corresponding Gaussian functions (blue circles).*

2.3. Simulating the Second Harmonic Generation Process

In this section I simulate the recently performed experiment [9] by numerically solving Eqs. (1.5) using the nonlinear current density described in Eq. (2.2). The numerical calculation is performed by using the fast-Fourier-transform method with respect to variables x and t and an integration with respect to z. We assume that the wavelength is 1.7 Å (7.3 keV), the polarization is parallel to the scattering plane (π-polarized), the pulse total energy is 4.3 μJ, the FWHM bandwidth is 1 eV, and the symmetric Gaussian FWHM waist is 1.5 μm. The nonlinear medium is a 0.5 mm long diamond crystal, with the pump focused at its middle. We choose to work in a symmetrical Laue geometry and phase-match the nonlinear process with the (2 2 0) reciprocal vector, which is parallel to the entrance and exit surfaces. In Fig. 2.2 we plot the efficiency of this process η_{sh}, defined as the total output SH signal-energy divided by the total input pump-energy, as a function of the propagation distance, and rocking curves, using the different models. Comparing these calculations to the experimental results [9], we find that the two broadened structures (LC and stochastic), with an assumed 20 fs FWHM duration, are adequately in agreement with the measured values. We see that the Bragg scattering process of the SH generated mode is negligible, since both the effective interaction length between the two modes and the coherence length arising from the nonzero phase mismatch $\Delta\vec{k}_B$ are much shorter than the extinction length of the elastic scattering process.

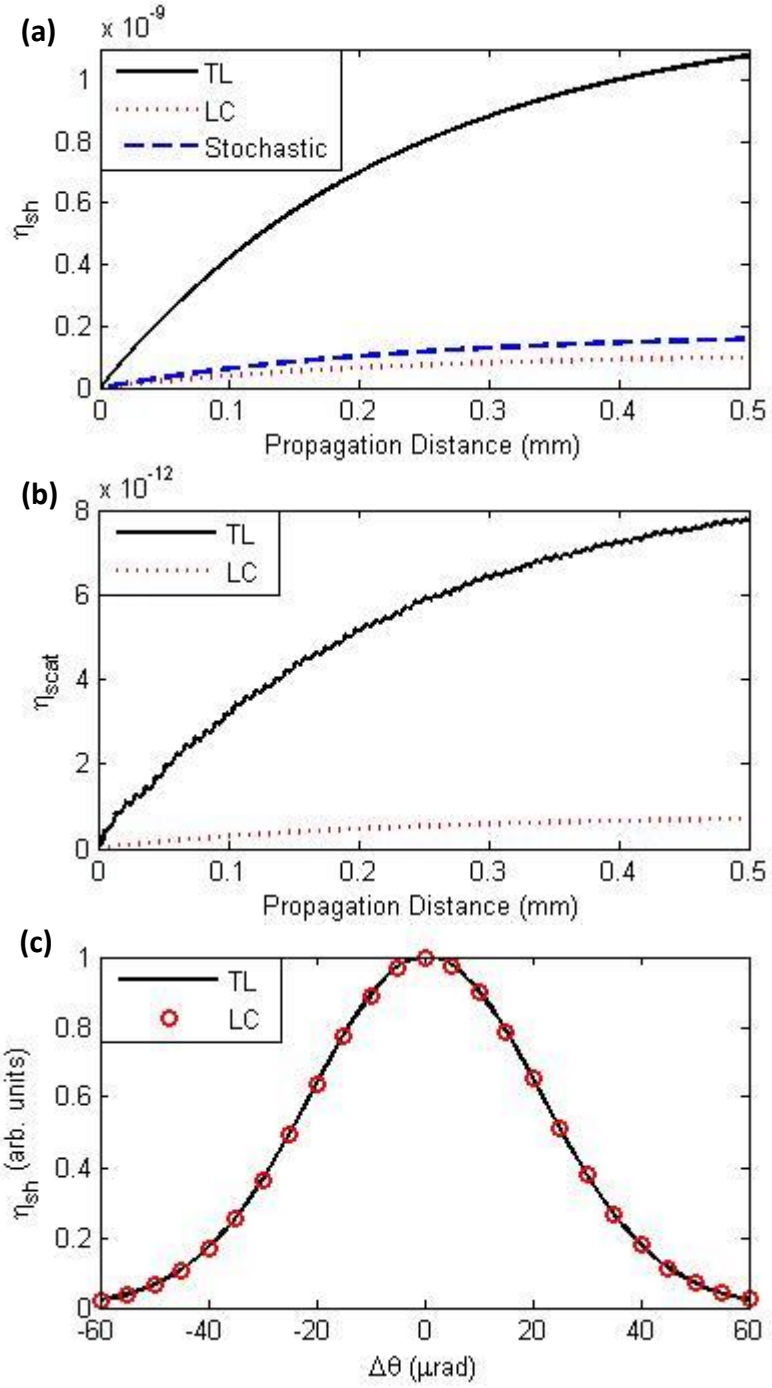

FIG. 2.2. SHG efficiencies and rocking curves for different pump models. ***(a)*** *and* ***(b)*** *show the efficiencies of the generated SH and its elastically scattered mode, respectively, as a function of propagation distance for the experiment parameters at perfect phase-matching, assuming a transform limited (TL, black solid lines), linearly chirped with 20 fs FWHM duration (LC, red dotted lines), and temporally-stochastic with 20 fs FWHM average duration (blue dot-dashed lines, averaged over 200 realizations) Gaussian pump pulses. The simulations for the stochastic pulses were*

performed assuming a negligible Bragg scattering. ***(c)*** *The SHG efficiency dependence on the deviation of the pump beam from the phase-matched angle* $\Delta\theta$*. Using normalized units, the two rocking curves are identical.*

From Eqs. (1.5) one notices that for short propagation distances, where the second term on the right hand side of Eq. (1.5a) is much smaller than the first term, an optimal coupling between the pump beam and the scattered SH mode occurs for $\Delta\vec{k}_{NL} = \Delta\vec{k}_B$. However, due to the dispersion, this relation between the two phase mismatch vectors does not occur.

As mentioned, due to the weak nonlinear susceptibility, it is necessary to focus the pump beam in order to get higher SH signal for a given pump pulse-energy. However, since the focused pump and the generated SH signal propagate in different directions with an angle $\rho = \theta_p + \theta_{sh}$ between them, they have a finite distance L_s within they overlap, causing spatial walk-off. Furthermore, the group velocity mismatch $GVM = \frac{1}{v_g(2\omega_0)\cos(\rho)} - \frac{1}{v_g(\omega_0)}$, results in a finite distance L_t within ultra-short pulses overlap, which causes temporal walk-off after a finite time.

As known in conventional nonlinear optics [7], affected only by diffraction, focusing the pump in the direction normal to the scattering plane does not introduce walk-off effects, therefore increasing the SHG efficiency by $\sim w_{0,y}^{-1}$, as long as the crystal length is shorter than the confocal parameter. However, reducing the beam size in the scattering plane results with a shorter effective interaction length. Fig. 2.3

shows the SHG efficiency dependence on focusing the pump pulse in the scattering plane $w_{0,x}$ for the experiment parameters. Here, as it will be explained in the next section, the SHG efficiency goes to a constant value as the beam waist decreases due to walk-off. Focusing further more decreases the efficiency due to diffraction, as in usual SHG of focused beams.

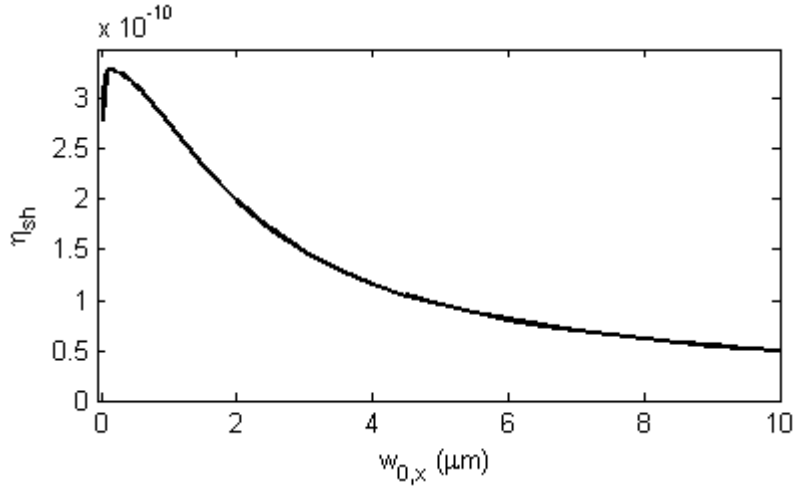

FIG. 2.3. Efficiency dependence on focusing in the scattering plane. *Using the parameters described in section 2.3 for a* $50\ \mu\mathrm{m}$ *crystal and a TL pulse. While diffraction-related effects limit the efficiency increment by focusing in the direction normal to the scattering plane, focusing in a direction parallel to the scattering plane reduces the effective interaction length, therefore decreases the SHG efficiency.*

2.4. Approximated Analytical Expressions

In order to describe the efficiency dependence upon the different parameters, analytical calculations of the overall SHG efficiency and tolerances are shown in the following section, compared with the numerical results of the pervious section. Wang et al. [10] developed a theoretical framework for calculating the efficiency of type-I SHG by tightly focused and ultra-short pulses with simultaneous spatial and

temporal walk-offs, generalizing pervious work by Boyd et al. [12]. This process may be considered analogues to our problem.

Using their approach, I solve the propagation aspects of our problem in the regime of negligible Bragg scattering of the SH generated wave.
In the case of negligible scattering of the SH wave, we are left to solve only Eq. (1.5a) without the second term on the right hand side. This type of propagation problem, where the generated SH propagates in a different direction than the pump beam, occurs in type-I SHG, where instead of a noncollinear phase-matching scheme determined by the reciprocal vector $\vec{G}$, the different propagation directions of the pump and SH beams arise from the different directions of the Poynting and wave vectors related to the extraordinary polarized SH mode. Therefore, both propagation problems have a similar form.

As shown in Ref. [10], it is possible to analytically evaluate partially, and under some assumptions, completely, the efficiency of the SHG process. For a small walk-off angle $\rho = \theta_p + \theta_{sh}$, the SH efficiency is (see derivation in Appendix):

$$\eta_{sh} = \frac{U_{sh}}{U_p} = \frac{\gamma U_p}{\sqrt{\pi} w_{0,x} w_{0,y} \tau} \int_0^{\frac{L}{\cos(\theta_p)}} \int_0^{\frac{L}{\cos(\theta_p)}} \frac{\exp\left(i\Delta k\left(z_1 - z_2\right)\right)\exp\left(-\frac{\left(z_1 - z_2\right)^2}{L_{s-t}^2}\right) dz_1 dz_2}{\sqrt{\left(1 - i\tau_x\left(z_1\right)\right)\left(1 - i\tau_y\left(z_1\right)\right)\left(1 + i\tau_x\left(z_2\right)\right)\left(1 + i\tau_y\left(z_2\right)\right)}}.$$

(2.5)

Where $\gamma = \frac{\omega_0^2}{2\pi n_p^2 n_{sh} \varepsilon_0 c^3} \left|\chi^{(2)}\left(2\omega_0; \omega_0, \omega_0\right)\right|^2$, U_p is the pump pulse total energy and L is the crystal length, assuming a symmetrical Laue geometry. We choose to take

the SHG phase mismatch $\Delta k = \left|\Delta \vec{k}_{NL}\right|$ normal to the boundary surface. The characteristic length within the pump and generated SH overlap, the spatiotemporal walk-off length, is defined as:

$$L_{s-t} = \left(\frac{\tan^2(\rho)}{w_{0,x}^2} + \frac{\zeta^2 + 1}{\tau^2} GVM^2 \right)^{-1/2} . \tag{2.6}$$

L_{s-t} represents an effective walk-off length which takes into account both causes of the limited interaction length between the pump and generated SH waves. The value of $\frac{\zeta^2 + 1}{\tau^2}$ remains constant for a given bandwidth ΔE. Therefore, observing Eq. (2.6), one notes that the interaction length L_{s-t} is limited by the coherence time of the pulse, which is inversely proportional to ΔE.

Assuming the focusing is weak enough so the confocal parameters are much larger than the crystal length $b_x, b_y \gg L$ and that the focal points $z_{0,x}$, $z_{0,y}$ are inside the crystal, Eq. (2.5) is simplified and the double integral may be presented in the form of error functions $erf(x)$:

$$\begin{aligned} \eta_{sh} &= \frac{\gamma U_p}{\sqrt{\pi} w_{0,x} w_{0,y} \tau} \int_0^{\frac{L}{\cos(\theta_p)}} \int_0^{\frac{L}{\cos(\theta_p)}} \exp\left(i\Delta k \left(z_1 - z_2\right)\right) \exp\left(-\frac{\left(z_1 - z_2\right)^2}{L_{s-t}^2} \right) dz_1 dz_2 = \\ &\frac{\gamma U_p L_{s-t}}{2\sqrt{\pi} w_{0,x} w_{0,y} \tau} e^{-\frac{1}{4}\Delta k^2 L_{s-t}^2} \left\{ L_{s-t} \left[e^{-\frac{\delta_+^2}{L_{s-t}^2}} + e^{-\frac{\delta_-^2}{L_{s-t}^2}} - 2e^{\frac{1}{4}\Delta k^2 L_{s-t}^2} \right] \right. \\ &\left. + \sqrt{\pi} \left[\delta_- erf\left(\frac{\delta_-}{L_{s-t}} \right) + \delta_+ erf\left(\frac{\delta_+}{L_{s-t}} \right) - i\Delta k \cdot L_{s-t}^2 erf\left(\frac{i}{2} \Delta k \cdot L_{s-t} \right) \right] \right\}, \end{aligned} \tag{2.7}$$

where $\delta_{\pm} = \frac{L}{\cos\left(\theta_p\right)} \pm \frac{i}{2}\Delta k \cdot L_{s-t}^2$.

In order to achieve higher SH signal, it is useful to take the crystal length L to be as long as a few absorption lengths of the pump pulse. Thus, for focused pump pulses with frequencies well above resonances, so absorption length is relatively large, it is worthwhile to study the regime of $L \gg L_{s-t}$. Assuming also $L \gg L_{s-t}^2 \Delta k$, Eq. (2.7) is reduced to a simplified expression:

$$\eta_{sh} = \frac{\gamma U_p L_{s-t} L}{w_{0,x} w_{0,y} \tau \cos\left(\theta_p\right)} \exp\left[-\left(\frac{\Delta k L_{s-t}}{2}\right)^2\right]. \qquad (2.8)$$

The efficiency grows linearly with the propagation length, as opposed to quadratically as in the case of phase-matched SHG without walk-off between the pump and the generated SH [7]. This effect, which is known in conventional nonlinear optics, may be explained by the fact that after each effective interaction length L_{s-t}, the pump pulse propagates away from the previously generated SH wave, thus the coherent accumulation of the generated SH signal begins all over again (see Fig. 2.4). The signal generated at each interaction length L_{s-t} sums up as the pump pulse propagates through the nonlinear medium, hence the linear dependence upon the propagation length L in Eq. (2.8).

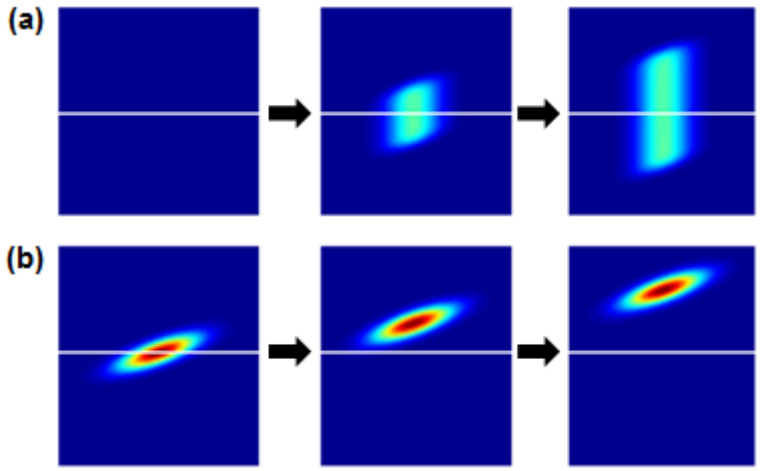

FIG. 2.4. Propagation aspects of the SHG process. ***(a)*** *and* ***(b)*** *show the evolution of the SH and pump pulses, respectively. After each walk-off length, the generated SH propagates in a different direction than the pump pulse, so the accumulation of the SH field does not continue.*

From Eqs. (2.6) and (2.8) we also note that as the beam waist in the direction parallel to the scattering plane $w_{0,x}$ decreases, the efficiency goes to a constant value, as shown in Fig. 2.3. A similar argument may be described for τ. We note that for further focusing, where $b_x, b_y \gg L$ does not hold, the efficiency decreases due to diffraction.

Under the previous assumptions of $L \gg L_{s-t}$ and $b_x, b_y \gg L$, and in perfect phase-matching condition $\Delta k = 0$, we consider in the SHG efficiency estimation the effect of absorption of the pump pulse propagating throughout the nonlinear media. In this regime, as shown in Eq. (2.8), the efficiency grows linearly with the pump pulse-energy and with the crystal length. Therefore, we modify Eq. (2.8) by including the exponential decay of the pump pulse over its propagation path, as follows:

$$\eta_{sh} = \frac{\gamma L_{s-t}}{w_{0,x} w_{0,y} \tau} \int_0^{\frac{L}{\cos(\theta_p)}} U_p \exp\left(-2\alpha_p z'\right) dz' = \frac{\gamma U_p L_{s-t}}{2\alpha_p w_{0,x} w_{0,y} \tau} \left[1 - \exp\left(-\frac{2\alpha_p L}{\cos(\theta_p)}\right)\right], \quad (2.9)$$

where α_p is the field absorption coefficient.

Fig. 2.5 shows the efficiency dependence on pump photon energy calculated both numerically and by using Eq. (2.9). As expected, the higher the pump photon energy (resulting in a smaller walk-off angle), the better the approximation holds. However, even with lower and more relevant photon energies, this simple analytical expression gives a decent estimation for the expected efficiency.

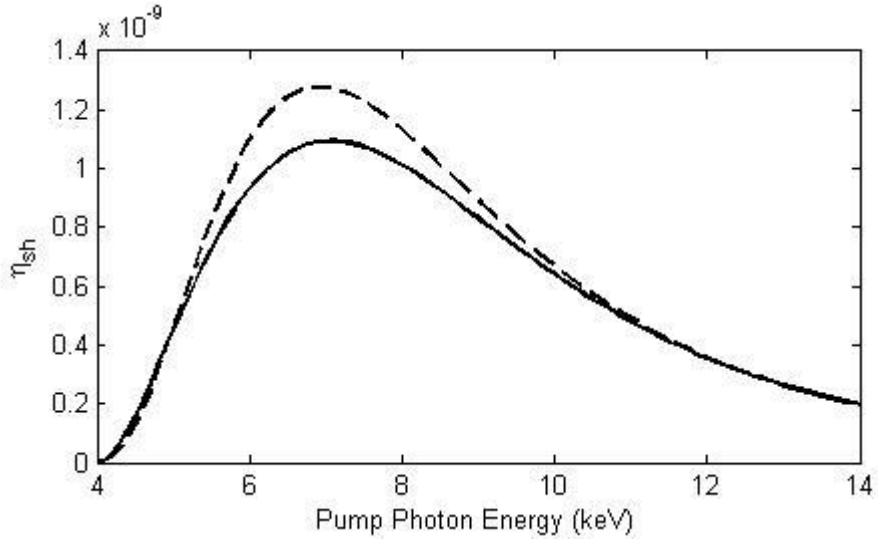

FIG. 2.5. Comparison between numerical simulations (solid line) and the approximated analytical expression (dashed line) for different pump photon energies. *Using the parameters of section 2.3, a TL pump structure and* $L = 0.5$ mm*, the analytical expression converges to the numerical result at high photon energies, where the walk-off angle decreases.*

I now address the rocking curve, or the angular acceptance bandwidth, of the SHG process. The phase-matching scheme of this process is similar to the one in quasi-phase-matching by periodically poled devices. In their study of tuning and tolerances of this process, Fejer et al. [13] derived the tolerance of the SHG efficiency to any parameter the phase mismatch Δk depends on.

From equation (2.8), we observe that the efficiency reduces to half of its perfectly phased-matched value when $\exp\left[-\left(\frac{\Delta k L_{s-t}}{2}\right)^2\right]=\frac{1}{2}$ is satisfied. Therefore, the mismatch $\Delta k'$ for which the SHG process will be half as efficient as the phase matched case is

$$\Delta k' = \frac{2\sqrt{\ln 2}}{L_{s-t}}. \tag{2.10}$$

Thus, in order to achieve an efficient SHG process, the coherence length, which is proportional to Δk^{-1}, should be as long as the effective interaction length.

Following [13], we expand the mismatch Δk dependence on the pump angle θ_p to first order $\Delta k\left(\theta_p\right)=\left(\theta_p-\theta_{p,0}\right)\left.\frac{\partial \Delta k}{\partial \theta_p}\right|_{\theta_p=\theta_{p,0}}$, where $\theta_{p,0}$ is the angle of the pump beam at perfect phase-matching. Using Eq. (2.10), the FWHM of the rocking curve $\Delta\theta_{p,FWHM}$ is therefore $\Delta\theta_{p,FWHM}=\frac{4\sqrt{\ln 2}}{L_{s-t}}\left|\frac{\partial \Delta k}{\partial \theta_p}\right|^{-1}_{\theta_p=\theta_{p,0}}$. Using Eqs. (A.8) for the phase mismatch, we derive by the geometry of the phase-matching scheme that

$\left.\frac{\partial \Delta k}{\partial \theta_p}\right|_{\theta_p=\theta_{p,0}} = 2k_p \tan\left(\theta_{p,0}+\theta_{sh,0}\right)$, where $\theta_{sh,0}$ is the SH angle at perfect phase-matching. Since the dispersion in x-ray frequencies is relatively weak, we may assume that the perfect phase-matching angles of the pump and SH beams are close to the Bragg angle of the SH frequency θ_B. Therefore, we find that the FWHM angle of the rocking curve is

$$\Delta\theta_{p,FWHM} = \frac{2\sqrt{\ln 2}}{k_p L_{s-t} \tan\left(2\theta_B\right)}. \tag{2.11}$$

Assuming the parameters in section 2.3, we get $\Delta\theta_{p,FWHM} = 49.5\ \mu rad$, which is in good agreement with Fig. 2.2(c). Since both the TL and LC pump structures of the same bandwidth have the same walk-off length L_{s-t}, their rocking curves are similar, as demonstrated in Fig. 2.2(c).

The phase-matching bandwidth of the SHG process is derived in a similar manner. We expand the dependence of the mismatch Δk on the pump frequency ω_0 to first order $\Delta k\left(\omega_0\right) = \left(\omega_0-\omega_c\right)\left.\frac{\partial \Delta k}{\partial \omega_0}\right|_{\omega_0=\omega_c}$, where ω_c is the central pump frequency for which there is perfect phase-matching. Assuming weak dispersion $\frac{\partial n\left(\omega_0\right)}{\partial \omega_0}=0$ and again using Eqs. (A.8), we get $\left.\frac{\partial \Delta k}{\partial \omega_0}\right|_{\omega_0=\omega_c} = \frac{2}{c}\left[n\left(\omega_c\right)-\frac{n\left(2\omega_c\right)}{\cos\left(\theta_{p,0}+\theta_{sh,0}\right)}\right]$. Taking both perfect phase-matching angles $\theta_{p,0}$, $\theta_{sh,0}$ as θ_B, and, furthermore, taking the indices of refraction at both the pump and SH frequencies as unity, we get the FWHM phase-matching bandwidth

$$\Delta\omega_{FWHM} = \frac{\sqrt{\ln 2}\cos(2\theta_B)c}{L_{s-t}\sin^2(\theta_B)}, \tag{2.12}$$

giving a value of 1.53×10^{15} Hz (1 eV) for the parameters in section 2.3, which is confirmed with an additional simulation. The dispersion has very little influence on the phase-matching bandwidth, which is determined mainly by the noncollinear nature of the phase-matching scheme.

It is possible to broaden the phase-matching bandwidth by replacing the perfect crystal with an imperfect crystal having a certain mosaic spread. As in linear Bragg diffraction, the angular distribution of the atomic planes throughout the crystal leads to a broader bandwidth since more frequencies of the incoming beam are able to be phase-matched at a certain point along the crystal. This broadening comes in the expanse of the peak diffraction efficiency. This effect has been verified by further simulations, assuming the crystal is composed from thin slabs of length Δz_0 that are infinite in the x-y direction and considered by themselves as perfect crystals. Assuming a Gaussian angular distribution, we randomly vary the direction of the reciprocal vector $\vec{G}$ between each slab. As expected, for a given angular distribution of the mosaic spread, the optimal SHG efficiency occurs when the slab thickness Δz_0 is on the order of the effective interaction length L_{s-t} or larger, where the phase-matched part of the pump spectrum coherently contributes to the generated SH field as if it was propagating in a perfect crystal.

2.5. Summary

In summary, this work analyzed the process of SHG at x-ray wavelengths from short and focused pulses. Modeling the input pump pulse using both deterministic and random spiky pulse structures, I simulated a recently performed experiment observing SHG using a pump pulse from an XFEL and showed good agreement with the experimental results. In addition, I studied several general aspects regarding the efficiency optimization and tolerances of the x-ray SHG process. Since the nature of the nonlinearity causes the pump and SH to propagate in different directions, the finite interaction distance between them may limit the efficiency increasement when focusing in a direction parallel to the scattering plane. However, this consideration does not affect the efficiency growth by focusing in the direction normal to the scattering plane, which is effective until the confocal parameter is in the order of the crystal length. Finally, under the assumptions of negligible elastic Bragg scattering of the generated SH, which we found to be reasonable in the case of the recently performed experiment, and small scattering angles, we showed simple analytical expressions for the total efficiency, rocking curve width, and phase-matching bandwidth of the SHG process.

3. X-Ray-Pulse Characterization by Spectral Shearing Interferometry Using Three-Wave Mixing

The intense ultrashort pulses generated by XFELs have opened new possibilities for probing and imaging structures and dynamics of matters on a time scale of tens of femtoseconds [14-17]. Indeed, the number of experiments and theoretical studies relying on ultrashort pulses at x-ray wavelengths is growing rapidly. Complete pulse characterization, including both amplitude and phase, could be essential when analyzing the results of those experiments. For example, intense x-ray spikes can modify the electronic configuration in matter via photoabsorption and recombination processes occurring on a femtosecond time scale [18]. Since any pulse emerging from a self-amplified spontaneous emission- (SASE) based XFEL contains a large number of randomly distributed spikes over a duration of several femtoseconds, the electrons do not return to their original configuration between the spikes. Consequently, the interpretation of the ultrafast electronic response to x-ray pulses requires the knowledge of the temporal structure of the pulses. In addition, the understanding of the temporal structure of the pulses emerging from the XFELs will improve their performances in a manner similar to the contributions of ultrafast diagnostic techniques to lasers in the optical regime. Other fields where the phase variation in the pulse and its temporal coherence are important are related to coherent processes in both electronic and nuclear interactions with x-rays [19,20].

Methods for the full characterization of ultrashort pulses have been shown to be very successful in a broad spectral range from infrared wavelengths to ultraviolet

wavelengths. Methods such as frequency-resolved optical gating (FROG), spectral interferometry for direct electric-field reconstruction (SPIDER) and their variations, have been highly successful in complete characterization of ultrashort pulses [21,22]. Many of these methods rely on the rapid nonlinear response of electrons in materials as an essential component in their scheme.

Unfortunately, nonlinear processes, such as second-harmonic generation [9] and two-photon absorption [23], are very weak in the x-ray regime. In addition, the random and spiky nature of the XFEL pulses requires single-shot characterization of the temporal structure. Thus in the absence of detectors with subfemtosecond response times, the temporal characterization of x-ray pulses is extremely difficult.

Several methods have been proposed or demonstrated for the characterization of x-ray pulses. Some approaches involve the same electron beam used for the generation of the XFEL radiation, in which its energy loss and spread are temporally resolved [24] or the electron beam is cross correlated with the x-ray field [25]. Another approach is a terahertz streaking measurement technique in which single-cycle terahertz pulses are used in order to spectrally broaden the kinetic-energy distribution of photoelectrons ejected by the x-ray pulse, having its temporal profile [26]. However, those methods do not provide phase information, and their temporal resolution is limited to above the few hundred attosecond pulse duration predicted for SASE XFEL spikes.

In this chapter, I propose a method for the measurement of the full temporal structure of x-ray pulses. Like other schemes based on spectral shearing interferometry, the proposed scheme is inherently applicable for single-shot

measurements, and the algorithm for the reconstruction of the temporal structure is straightforward. In essence, in this scheme the measured x-ray pulse is mixed with two synchronized optical pulses at different frequencies in the same nonlinear medium to generate two spectrally shifted pulses. The two spectrally shifted replicas of the incident pulse form a spectral interference pattern, which is resolved by a single-shot spectrometer. The generation of the two replicas can be performed by using the effect of x-ray and optical wave mixing [27]. This recently observed effect is about four orders of magnitude stronger than other wave-mixing effects when all pertinent wavelengths are in the x-ray regime. Of importance, since the intensity of the generated signal scales linearly with the intensity of the optical and x-rays fields, and since high power optical lasers are available today, the effect can be observed with all pertinent beams unfocused and with optical pulse durations of several picoseconds. Hence this scheme is independent of the jitter of the x-ray pulses, and the spatiotemporal phase distortion during the nonlinear process due to focusing is minimized.

3.1. Retrieving the Spectral Phase

The temporal pulse structure $E(t)$ can be fully represented by its spectrum via a Fourier transform, namely, $\tilde{E}(\omega) = A(\omega)e^{i\varphi(\omega)}$. Here $A(\omega)$ is the spectral amplitude, and $\varphi(\omega)$ is the spectral phase. Consequently, the full characterization of ultrashort pulses can be obtained by the measurements of both the spectral amplitude and the spectral phase of the electric field. The measurement of the spectral amplitude is relatively easy and usually is performed by using a

spectrometer with a slow detector, which is an advantage when characterizing ultrashort pulses having a temporal duration shorter than the possible electronic response time. The measurement of the spectral phase is more challenging since interferometric measurements using linear optical components and slow detectors measure only the power spectrum of the pulse. In order to retrieve the spectral phase, spectral interference between two spectrally shifted replicas of the tested pulse is being used in devices based on SPIDER techniques [21,28]. Generally, the power spectrum of the superposition of two spectrally shifted replicas $\tilde{E}(\omega-\Omega_1)$ and $\tilde{E}(\omega-\Omega_2)$ of the test pulse has the form of

$$I(\omega)\sim\left|e^{i\phi_1}\tilde{E}(\omega-\Omega_1)+e^{i(\phi_2+\omega\tau)}\tilde{E}(\omega-\Omega_2)\right|^2=\left[A(\omega-\Omega_1)\right]^2+\left[A(\omega-\Omega_2)\right]^2 \\ +2A(\omega-\Omega_1)A(\omega-\Omega_2)\cos\left[\varphi(\omega-\Omega_1)-\varphi(\omega-\Omega_2)+\phi_1-\phi_2-\omega\tau\right]. \quad (3.1)$$

Where Ω_1 and Ω_2 are the spectral shift of each of the replicas, ϕ_1 and ϕ_2 are the global phase of each replica, and τ is a possible temporal delay between them. Extracting $\varphi(\omega-\Omega_1)-\varphi(\omega-\Omega_2)$, one obtains the phase difference between spectral components $\Delta\Omega=\Omega_2-\Omega_1$ apart. In essence, spectral shearing interferometry converts spectral phase information to spectral amplitude information, which is easier to measure. This straightforward noniterative reconstruction process gives the pulse spectrum at sequential points $\tilde{E}(\omega_n)$, where $\omega_n=\omega_0+\Delta\Omega n$ with ω_0 being a certain starting point. For pulses with compact support over a duration of T, the Nyquist-Shannon sampling theorem states that, if the sampling in the spectral domain is carried out with an interval of $\Delta\Omega\le\frac{2\pi}{T}$, the

original pulse $E(t)$ may be fully reconstructed. Note that since only phase differences between sequential points are measured, this method does not account for the global phase and the pulse arrival time.

3.2. Spectral Shearing via X-Ray and Optical Wave Mixing

The scheme proposed in this work is based on the spectral interference between two frequency-shifted signals. One possible way to generate these signals in the x-ray regime is to use the effect of x-ray and visible wave mixing. Here the x-ray pulse (with a central angular frequency ω_x) is mixed with two nearly monochromatic optical pulses with central angular frequencies Ω_1 and Ω_2. Their frequency difference $\Delta\Omega$ corresponds to the shift required for the spectral interference pattern. By observing the different terms in Eq. (1.3), it has been shown by Glover et al. [27] that in the x-ray and optical wave-mixing process, the dominant contribution to the nonlinear current density is the Doppler term, originated from the inelastic scattering of the x-ray field by the optically induced charge distribution:

$$\vec{J}^{(2)}_{\omega_x+\Omega_{1/2}}(\vec{r},t)=\hat{\rho}^{(1)}_{\vec{G},\Omega_{1/2}}\vec{v}^{(1)}_{\omega_x}=\frac{iq}{4m_e\omega_x}\rho^{(1)}_{\vec{G},\Omega_{1/2}}E_x(\vec{r},t)e^{i\left(\vec{k}_x+\vec{k}_{L,1/2}+\vec{G}\right)\cdot\vec{r}-i(\omega_x+\Omega_{1/2})t}\hat{e}_x+c.c. \quad (3.2)$$

Where $\vec{v}^{(1)}_{\omega_x}=\frac{iqE_x(\vec{r},t)}{2m_e\omega_x}e^{i\vec{k}_x\cdot\vec{r}-i\omega_x t}\hat{e}_x+c.c.$ is the first-order induced velocity by the x-ray field, the x-ray pump pulse and the optically induced charge distribution are written as an envelope times a carrier wave $\hat{E}_x(\vec{r},t)=\frac{1}{2}E_x(\vec{r},t)e^{i\vec{k}_x\cdot\vec{r}-i\omega_x t}\hat{e}_x+c.c.$,

$\hat{\rho}^{(1)}_{\vec{G},\Omega_{1/2}}(\vec{r},t)=\frac{1}{2}\rho^{(1)}_{\vec{G},\Omega_{1/2}}(\vec{r},t)e^{i\left(\vec{k}_{L,1/2}+\vec{G}\right)\cdot\vec{r}-i\Omega_{1/2}t}+c.c.$ $\vec{k}_x$ and $\vec{k}_{L,1/2}$ are the wave vectors of

the x-ray and the optical carrier fields, respectively, $\vec{G}$ is a specific reciprocal lattice vector, $\rho^{(1)}_{\vec{G},\Omega_{1/2}}$ is the $\vec{k}_{L,1/2}+\vec{G}$ spatial Fourier component of the optically induced charge distribution, m_e and q are the electron's mass and charge, respectively, and $\hat{e}_x$ is the x-ray pump polarization vector. We estimate the optically induced charge $\rho^{(1)}_{\vec{G},\Omega_{1/2}}$, which scales linearly with the IR or visible electric field, by using the tabulated indices of refraction at Ω_1 and Ω_2.

3.3. The Proposed Scheme

I consider here a scheme in which the two frequency-shifted replicas are generated in the same nonlinear medium. This scheme minimizes the number of optical components, such as beam splitters and mirrors, required for the inspection of the pulse structure. A sketch of a possible setup for x-ray pulse characterization by spectral shearing interferometry using one nonlinear medium is shown in Fig. 3.1(a). Since the frequency shifts of the two generated replicas are different, they propagate in different directions, imposed by the phase-matching conditions as described in Fig. 3.1(b). However, since the k-vector of the optical wave is much smaller than the k-vectors of the x-ray waves and since dispersion in the x-ray regime is relatively weak, there are two possible approaches in which the spectral interference pattern could be obtained without additional x-ray optical components. The first approach it to impose that the two frequency-shifted replicas propagate in the same direction by simultaneous optimization of the phase mismatch for both frequency mixing processes. Both sum-frequency generation (SFG) signals would propagate efficiently in the same direction as long as the crystal length is smaller

than the coherence lengths of both processes. The second approach, which I choose for the following analysis, is to use the smallest possible angle between the two SFG beams while keeping the exact phase-matching conditions for both mixing processes. When using the second approach, a spatial fringe pattern is added to the interference pattern described in Eq. (3.1). Fortunately, it is easy to generalize Eq. (3.1) to include this spatial fringe pattern, which is a simple oscillatory function in the case of no transverse phase variations. In the case where the measured pulse is not a plane wave, the spectral phase retrieval requires the knowledge of the spatial structure of the pulse. Also, one should note that the extraction of the phase difference $\varphi(\omega-\Omega_1)-\varphi(\omega-\Omega_2)$ is possible only when the phase between the two SFG beams is locked to a known value [29]. In addition, the third term of Eq. (3.1) should not be an even function of $\varphi(\omega-\Omega_1)-\varphi(\omega-\Omega_2)$, otherwise the sign of the requested phase difference cannot be resolved. Therefore, it is assumed that $\phi_1-\phi_2=\frac{\pi}{2}$ for the following analysis.

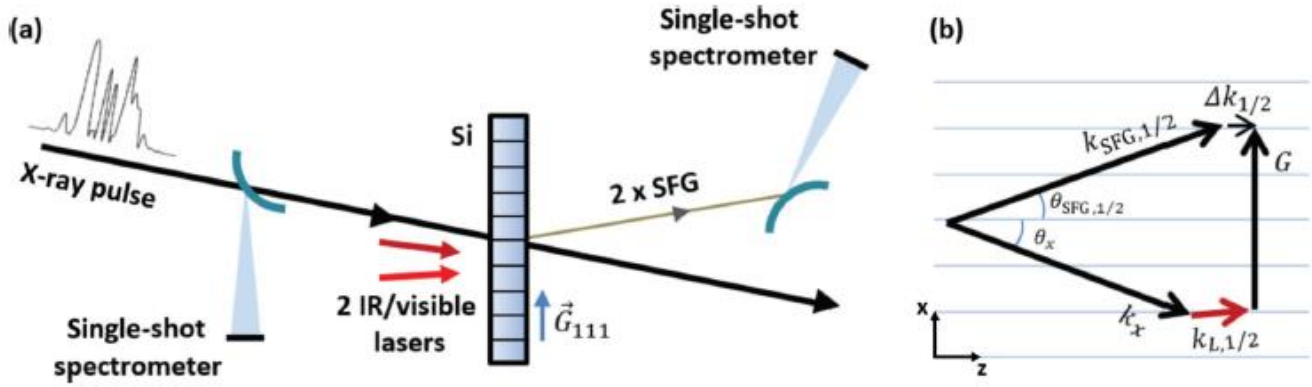

FIG. 3.1. (a) Schematic example of the spectral shearing interferometer. *A small fraction of the tested x-ray pulse is used for the measurement of its power spectrum. The pulse is mixed with two lasers with different optical frequencies in a nonlinear crystal. The generated signal is spectrally resolved to give the spectral shearing interference pattern from which the phase difference between neighboring spectral components is deduced.* **(b)** Phase-matching diagram for the two SFG processes. *The mismatch vector for each process is defined as* $\Delta\vec{k}_{1/2} = \vec{k}_x + \vec{k}_{L,1/2} + \vec{G} - \vec{k}_{SFG,1/2}$.

3.4. Simulating the Generated Interference Pattern

In this section I numerically solve the propagation equations describing the generation of the spectral interference pattern. The electric fields of the sum-frequency generated signals are written as an envelope times a carrier wave $\hat{E}_{SFG,1/2}(\vec{r},t) = \frac{1}{2}E_{SFG,1/2}(\vec{r},t)e^{i\vec{k}_{SFG,1/2}\cdot\vec{r}-i(\omega_x+\Omega_{1/2})t}\hat{e}_{SFG,1/2} + c.c.$. The phase-matching conditions are $\Delta\vec{k}_{1/2} = \vec{k}_x + \vec{k}_{L,1/2} + \vec{G} - \vec{k}_{SFG,1/2} = 0$. The slowly varying envelope equation for each of the SFG fields generated by the nonlinear current densities described in Eq. (3.2) is as follows:

$$\sin\left(\theta_{SFG,1/2}\right)\frac{\partial E_{SFG,1/2}}{\partial x}+\cos\left(\theta_{SFG,1/2}\right)\frac{\partial E_{SFG,1/2}}{\partial z}+\frac{1}{v_{g,1/2}}\frac{\partial E_{SFG,1/2}}{\partial t}= -\frac{i\eta_{1,2}q}{4m_e\omega_x}\left(\hat{e}_x\cdot\hat{e}_{SFG,1/2}\right)\rho^{(1)}_{\vec{G},\Omega_{1/2}}E_x\left(\vec{r},t\right) \tag{3.3}$$

where $v_{g,1/2}$ and $\eta_{1,2}$ are the group velocity and the wave impedance inside the crystal at the frequency $\omega_x+\Omega_{1/2}$, respectively. x and z are the coordinated in the scattering plane parallel and normal to the crystal surface, respectively. The k-vectors of the pertinent beams are chosen to satisfy the exact phase-matching conditions for both mixing processes, where the two SFG fields are generated in the very nearly same direction.

Eq. (3.3) is numerically solved by the fast-Fourier-transform method with respect to variables x and t and an integration with respect to z. The considered nonlinear medium is a perfect silicon crystal. We assume that the (111) reflection is used to achieve phase-matching and that the thickness of the crystal is $10\ \mu m$. Stochastic test pulses as described in section (2.2) are assumed, having for simplicity a symmetric Gaussian (TEM_{00}) shape for the transverse field. We assume the average FWHM bandwidth of these pulses is $1\ eV$ centered at $10\ \mathrm{k}eV$, the average FWHM duration is $20\ fs$, the beam FWHM waist is $100\ \mu\mathrm{m}$, and the polarization direction is taken to be normal to the scattering plane. The x-ray pulses are mixed with two IR quasimonochromatic plane-wave beams at 1.88 and 1.91 $\mu\mathrm{m}$, both polarized in the scattering plane. The corresponding spectral distance between the optical pulses is $\Delta\Omega=0.01\ \mathrm{eV}$. The directions of propagation of the two lasers affect the efficiencies of the nonlinear processes (optimal with the polarization parallel to $\vec{G}$); the angle between the two SFG signals (which should be small in order to reduce the spatial

interference) and their deviation from the Bragg angle (which should be large in order to reduce the elastic scattering background of the test pulse). With the preference being a higher SFG efficiency and deviation from the Bragg angle than a smaller angle between the two SFG signals, both laser beams are assumed to be almost perpendicular to $\vec{G}$ as in Fig. 3.1. With exact phase matching for both nonlinear processes giving an angle of 2.8° between the two optical lasers, the angle between the propagation directions of the two SFG fields $\theta_{SFG,2} - \theta_{SFG,1}$ is $11.6\ \mu\text{rad}$, whereas their angular deviation from the Bragg angle is $413\ \mu\text{rad}$. The assumed optical pulses are of $1\,ps$ duration with a peak intensity of $10^{11}\ W/cm^2$, which is below the IR damage threshold of silicon [30]. It is important to note that with a pulse duration of $1\,ps$ and a crystal length of $10\ \mu m$, the GVM between the x-ray and the optical pulses is negligible. However, there is a GVM between the x-ray test pulse and the SFG field, which limits the phase-matching bandwidth of the nonlinear process. An example for the power spectrum of the SFG signal is shown in Fig. 3.2. For these parameters, the average efficiency of the x-ray and optical mixing is about 10^{-6}.

The full spectral interference pattern is distributed over an angular spread of about $30\ \mu rad$ since different angles satisfy phase-matching conditions for different portions of the pulse spectrum. This distribution constrains the angular tolerance of the single-shot spectrometer.

Using the spectral interference pattern and the power spectrum of the original test pulse, which could be obtained by an additional single-shot spectrometer as

shown in Fig. 3.1(a), the phase differences $\varphi(\omega-\Omega_1)-\varphi(\omega-\Omega_2)$ are extracted, from which the pulse spectrum (amplitude and phase) at sequential points $\tilde{E}(\omega_n)$ is calculated. Following that, an inverse Fourier transform of this spectrum is used to reconstruct the original temporal structure of the test pulse $E(t)$. An example of the reconstructed and the original temporal structures is shown in Fig. 3.3.

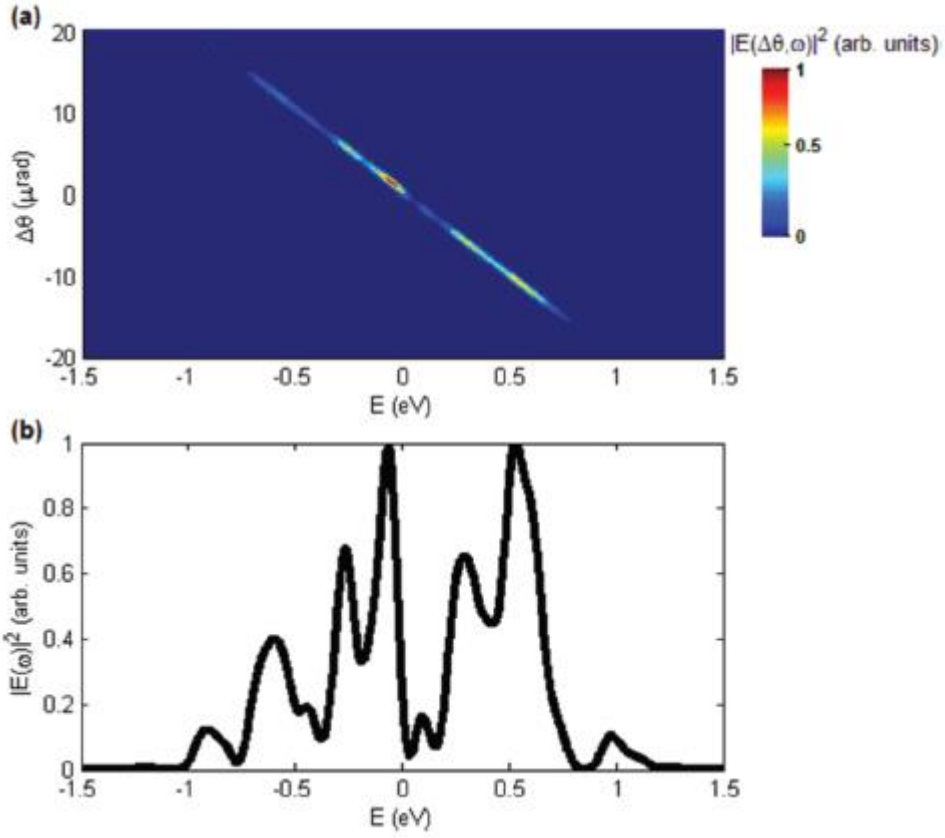

FIG. 3.2. An example of the power spectrum for a signal generated by the two SFG processes. ***(a)*** *The angular-spectral power distribution of the generated signal, showing the direction in which different portions of the spectrum propagate.* ***(b)*** *The power spectrum of the combined signal from the two generated SFG signals. This power spectrum portrays the concerning spectral interference pattern.*

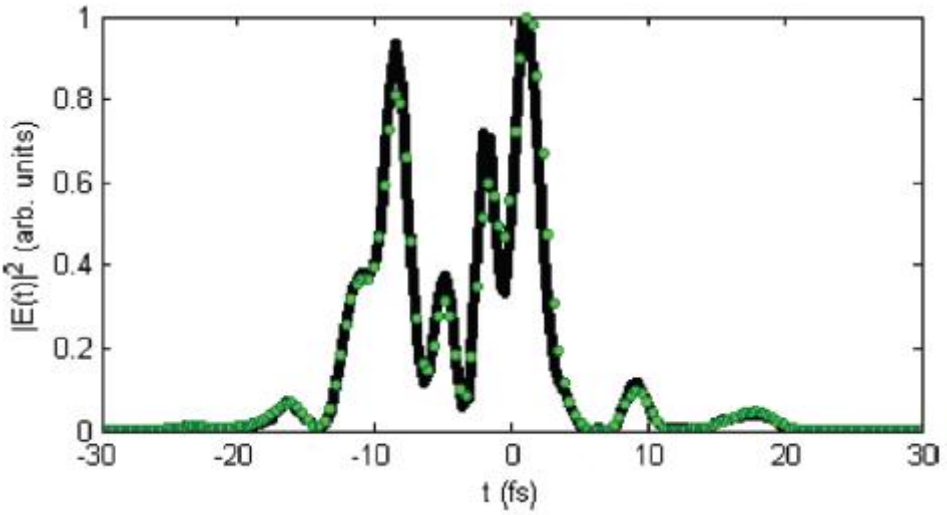

FIG. 3.3. Reconstruction of a random x-ray pulse. *The black solid line describes the temporal structure of a stochastic x-ray test pulse produced by the model described in section (2.2). The green dots describe the reconstruction from the spectral interference pattern [Fig. 3.2(b)], obtained for the test pulse by using two nonlinear mixing processes with optical lasers at 1.88 and 1.91* μm *as the shearing mechanism, the nonlinear medium being a 10-* μm *Si crystal, and by using the power spectrum of the tested pulse.*

3.5. Discussion

In this section the practical limitations and constraints of the proposed scheme are discussed. One of the major challenges is that the amplitudes and phases of the pulses emerging from XFELs fluctuate randomly. Thus, the temporal structure of different pulses is substantially different. Consequently, the measurement of the spectral interference pattern requires the use of a single-shot spectrometer with a resolution that is adequate to capture significant phase variations over the pulse spectrum. Fortunately, several successful schemes for the shot-by-shot

measurement of spiky XFEL pulses with spectral resolutions of 14 meV have been demonstrated [31-33].

A pulse-shape reconstruction is reliable only when the spectral interference of neighboring spectral components is revealed. The upper bound of the spectral difference $\Delta\Omega$ is limited by the Nyquist-Shannon sampling theorem. The lower bound of $\Delta\Omega$ is determined by the visibility of the interference and the ability of the apparatus to resolve the interference pattern. Furthermore, since only the phase differences between spectral components $\Delta\Omega$ apart are measured, the characterization is incomplete if the spectral amplitude $A(\omega)$ is zero over a frequency interval larger than the spectral difference $\Delta\Omega$. In these cases, an additional similar scheme having a spectral shear greater than this interval is required in order to achieve the full characterization of the spectral phase.

The efficiency of the SFG process increases with the crystal length. However, there are several restrictions on the practical crystal thickness that may be used for the spectral shearing. Since the coherence length of the nonlinear process is inversely proportional to the phase mismatch, a thin crystal is necessary to achieve a phase-matching bandwidth comparable to the bandwidth of the inspected pulses. In addition, spatial variations in the test pulses and the noncollinear geometry of the nonlinear process in thick crystals induce a spatiotemporal coupling, which adds distortions to the generated SFG fields, which thus blurs the temporal structure encoded in the interference pattern. These restrictions have been verified by further numerical simulations, varying the crystal thickness and assuming other diffraction planes, thus having different propagation geometries.

3.6. Summary

To summarize, I have described a method to fully characterize the temporal structure of ultrashort hard x-ray pulses. The method is based on the spectral interference between two sheared replicas of the original pulse, generated by three-wave mixing with IR or visible lasers. Practically, the scheme is limited by the efficiency and bandwidth of the x-ray and optical mixing process and by the performance of the single-shot spectrometer.

The proposed scheme has several important advantages: (1) It works on a single-shot basis and does not require moving parts. (2) The temporal jitter of the x-ray pulses does not influence the measurement since the duration of the optical pulses can be much longer than the maximum jitter. (3) The nonlinear medium can be a thin crystal to minimize propagation distortions of the tested pulse. (4) The measured quantities are only the power spectra of the tested pulse and its interfering replicas. (5) The retrieval algorithm of the pulse structure is straightforward, and the only ambiguities are the global phase and the pulse arrival time.

4. Outlook

The successful operation of XFELs, producing intense ultrashort x-ray pulses, has introduced a novel tool for the study of structure and dynamics of matter. The ongoing research utilizing XFEL radiation in physics, chemistry, and biology, has already provided fruitful results, which creates an increasing interest in XFEL science and its applications. Among the scientific fields that benefit from the use of XFELs, nonlinear x-ray optics has advanced considerably. Using XFEL radiation, fundamental nonlinear processes such as x-ray SHG [9], x-ray and optical wave mixing [27], and x-ray two-photon absorption [23], were observed.

The purpose of this thesis was to investigate two problems related to nonlinear x-ray optics. In chapter 2 a detailed study of x-ray SHG was shown, which addressed the unique differences of this process compared to conventional optical SHG. Further research regarding x-ray SHG may concern pulse inspection techniques, such as intensity autocorrelation, and additional modeling of the nonlinear response of matter to x-rays. Next, an x-ray pulse characterization technique based on spectral shearing interferometry, using x-ray and optical wave mixing as the shearing mechanism, was suggested in chapter 3. Pulse characterization techniques could become essential for the interpretation of ultrafast x-ray diffraction experiments. Furthermore, they may be used to improve the performances of XFELs in a manner similar to the characterization of ultrafast lasers in the optical regime. Further research regarding this approach may include the optimization of the nonlinear mixing process, considering, for example, different nonlinear media with stronger nonlinearity and higher damage threshold.

References

[1] A. Authier, *Dynamical Theory of X-Ray Diffraction* (Oxford University Press, New York, 2001).

[2] P. Eisenberger, and S. L. McCall, Phys. Rev. Lett. **26**, 684 (1971).

[3] K. Tamasaku, K. Sawada, E. Nishibori, and T. Ishikawa, Nat. Phys. **7**, 705 (2011).

[4] B.W. Adams, *Nonlinear Optics, Quantum Optics, and Ultrafast Phenomena with X-Rays* (Kluwer Academic Publisher, Norwell, MA, 2008).

[5] Y. R. Shen, *The principles of nonlinear optics* (Wiley, New York, 1984).

[6] A. Nazarkin, S. Podorov, I. Uschmann, E. Forster, and R. Sauerbrey, Phys. Rev. A **67**, 041804(R) (2003).

[7] R. Boyd, *Nonlinear Optics* (Academic, New York, 1992).

[8] P. A. Franken, A. E. Hill, C. W. Peters, and G. Weinreich, Phys. Rev. Lett. **7**, 118 (1961).

[9] S. Shwartz *et al.*, Phys. Rev. Lett. **112**, 163901 (2014).

[10] H. Wang and A. Weiner, IEEE J. Quantum Electron. **39**, 1600 (2003).

[11] S. D. Shastri, P. Zambianchi, and D. M. Mills, J. Synchrotron Radiat. **8**, 1131 (2001).

[12] G. D. Boyd and D. A. Kleinman, J. Appl. Phys. **39**, 3597 (1968).

[13] M. M. Fejer, G. A. Magel, D. H. Jundt, and R. L. Byer, IEEE J. Quantum Electron. **28**, 2631 (1992).

[14] R. Neutze, R. Wouts, D. van der Spoel, E. Weckert, and J. Hajdu, Nature (London) **406**, 752 (2000).

[15] K. J. Gaffney and H. N. Chapman, Science **316**, 1444 (2007).

[16] M. Trigo *et al.*, Nat. Phys. **9**, 790 (2013).

[17] J. Küpper *et al.*, Phys. Rev. Lett. **112**, 083002 (2014).

[18] L. Young *et al.*, Nature (London) **466**, 56 (2010).

[19] B. W. Adams *et al.*, J. Mod. Opt. **60**, 2 (2013).

[20] W.-T. Liao, A. Pálffy, C. H. Keitel, Phys. Rev. C **87**, 054609 (2013).

[21] I. A. Walmsley and C. Dorrer, Adv. Opt. Photonics **1**, 308 (2009).

[22] R. Trebino, *Frequency-Resolved Optical Grating: The Measurement of Ultrashort Laser Pulses* (Kluwer Academic, Boston, 2002).

[23] K. Tamasaku *et al.*, Nat. Photonics **8**, 313 (2014).

[24] Y. Ding, C. Behrens, P. Emma, J. Frisch, Z. Huang, H. Loos, P. Krejcik, and M-H. Wang, Phys. Rev. Spec. Top.- Accel. Beams **14**, 120701 (2011).

[25] Y. Ding *et al.*, Phys. Rev. Lett. **109**, 254802 (2012).

[26] I. Grguraš *et al.*, Nat. Photonics **6**, 852 (2012).

[27] T. E. Glover *et al.*, Nature (London) **488**, 603 (2012).

[28] C. Iaconis and I. A. Walmsley, Opt. Lett. **23**, 792 (1998).

[29] H. Miao, D. E. Leaird, C. Langrock, M. M. Fejer, and A. M. Weiner, Opt. Express **17**, 3381 (2009).

[30] B. M. Cowan, Proc. SPIE **6720**, 67201M (2007).

[31] D. Zhu, M. Cammarata, J. M. Feldkamp, D. M. Fritz, J. B. Hastings, S. Lee, H. T. Lemke, A. Robert, J. L. Turner, and Y. Feng, Appl. Phys. Lett. **101**, 034103 (2012).

[32] Y. Inubushi *et al.*, Phys. Rev. Lett. **109**, 144801 (2012).

[33] P. Karvinen *et al.*, Opt. Lett. **37**, 5073 (2012).

[34] N. Bloembergen, and P. Pershan, Phys. Rev. **128**, 606 (1962).

Related Publications

- S. Yudovich, and S. Shwartz, "X-ray-pulse characterization by spectral shearing interferometry using three-wave mixing", Physical Review A **90**, 033805 (2014).

- S. Shwartz, M. Fuchs, J. B. Hastings, Y. Inubushi, T. Ishikawa, T. Katayama, D. A. Reis, T. Sato, K. Tono, M. Yabashi, S. Yudovich, and S. E. Harris, "X-Ray Second Harmonic Generation", Physical Review Letters **112**, 163901 (2014).

- S. Yudovich, and S. Shwartz, "Second harmonic generation of focused ultrashort x-ray pulses", submitted.

Appendix: Derivation of Second Harmonic Generation Efficiency

In order to calculate the efficiency of the SHG process, I follow the work of Wang et al. [10]. In their paper, the authors analyzed SHG processes for focused and short pump pulses, using an ooe type-I phase matching scheme. In these processes the generated SH, which has an extraordinary polarization, propagates with a certain walk-off angle ρ relative to the ordinary polarized pump beam due to Poynting vector walk-off. This propagation problem is analogous to the one studied in this work, with the only difference being the origin of the spatial walk-off angle.

The pump and SH fields are defined as an envelope times a carrier wave $\vec{E}_p(\vec{r},t)=\frac{1}{2}E_p(\vec{r},t)e^{i\left(\vec{k}_p\cdot\vec{r}-\omega_0 t\right)}\hat{e}_p+c.c$, $\vec{E}_{sh}(\vec{r},t)=\frac{1}{2}E_{sh}(\vec{r},t)e^{i\left(\vec{k}_{sh}\cdot\vec{r}-2\omega_0 t\right)}\hat{e}_{sh}+c.c$. We assume a linearly chirped Gaussian envelope for the pump field, which propagates in the z direction (see Fig. A.1):

$$E_p(x,y,z,t)=\frac{E_0}{\sqrt{\left(1-i\tau_x(z)\right)\left(1-i\tau_y(z)\right)}}\times\exp\left(-\frac{x^2}{w_{0,x}^2\left(1-i\tau_x(z)\right)}-\frac{y^2}{w_{0,y}^2\left(1-i\tau_y(z)\right)}-\frac{(1+i\zeta)}{\tau^2}\left(t-\frac{z}{v_g(\omega_0)}\right)^2\right). \quad \text{(A.1)}$$

We define $\tau_x(z)=\frac{2\left(z-z_{0,x}\right)}{b_x}$ and $\tau_y(z)=\frac{2\left(z-z_{0,y}\right)}{b_y}$. $w_{0,x}$, $w_{0,\mathrm{y}}$ and τ determine the Gaussian pulse size and duration, respectively. $z_{0,x}$ and $z_{0,y}$ set the focal point,

ζ defines the linear chirp and $b_x = k(\omega_0) w_{0,x}^2$, $b_y = k(\omega_0) w_{0,y}^2$ are the confocal parameters inside the material.

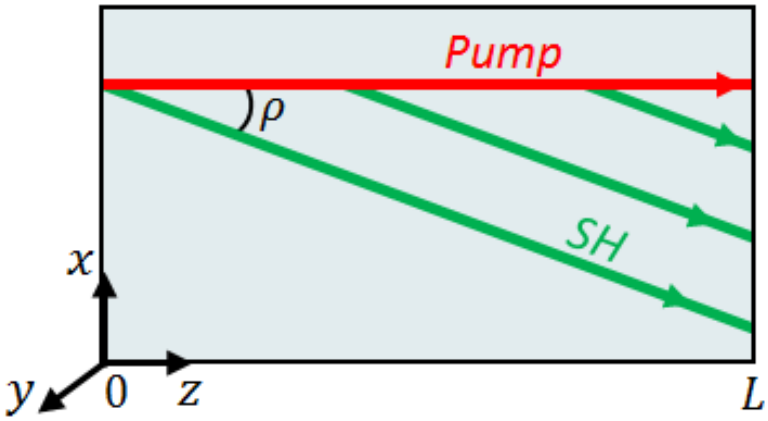

FIG. A.1. *The pump beam propagates parallel to the z direction at the group velocity* $v_g(\omega_0)$*, and generates SH field which propagates at the group velocity* $v_g(2\omega_0)$*, with some walk-off angle* ρ *from the pump.*

Since the pump beam generates SH field throughout its propagation inside the nonlinear crystal, we start by writing the infinitesimal increment of the SH field at some arbitrary point (x', y', z', t') [7]:

$$dE_{sh}(x', y', z', t') = i\kappa E_p^2(x', y', z', t')\exp(i\Delta k z')dz'. \quad \text{(A.2)}$$

Where $\kappa = \dfrac{\omega_0 \chi^{(2)}(2\omega_0; \omega_0, \omega_0)}{2n_{sh}c}$. By inserting the pump envelope (A.1) into Eq. (A.2) we get:

$$dE_{sh}\left(x',y',z',t'\right)=\frac{i\kappa E_0^2\exp\left(i\Delta kz'\right)dz'}{\sqrt{\left(1-i\tau_x\left(z'\right)\right)\left(1-i\tau_y\left(z'\right)\right)}}\exp\left(-\frac{2\left(1+i\zeta\right)}{\tau^2}\left(t'-\frac{z'}{v_g\left(\omega_0\right)}\right)^2\right)$$
$$\times\left\{\frac{1}{\sqrt{\left(1-i\tau_x\left(z'\right)\right)\left(1-i\tau_y\left(z'\right)\right)}}\exp\left(-\frac{2x'^2}{w_{0,x}^2\left(1-i\tau_x\left(z'\right)\right)}-\frac{2y'^2}{w_{0,y}^2\left(1-i\tau_y\left(z'\right)\right)}\right)\right\}.$$

(A.3)

Since the term in brackets may be identified as the Gaussian TEM_{00} solution for the paraxial wave equation, we propagate this field from z' to the output surface L by merely replacing $z'=\mathrm{L}$ within this term.

The generated SH field at each source point $\left(x',y',z',t'\right)$ will propagate towards the observer at its group velocity $v_g\left(2\omega_0\right)$ in a direction parallel to its Poynting vector. Therefore, an observer at a point on the output end of the crystal $\left(x,y,z=L,t\right)$ will see the SH field generated at $\left(x-(\mathrm{L}-\mathrm{z}')\tan\left(\rho\right),\ y,\ z',\ \mathrm{t}-\frac{L-z'}{v_g\left(2\omega_0\right)\cos\left(\rho\right)}\right)$ for $z'=\left[0,\mathrm{L}\right]$, as in Fig. A.1.

Using the paraxial approximation, we follow the last two arguments and integrate the infinitesimal SH field increment in Eq. (A.3) with respect to z'. Therefore, we obtain the observed SH field at $\left(x,y,L,t\right)$:

$$E_{sh}\left(x,y,\mathrm{L},t\right)=\frac{i\kappa E_0^2}{\sqrt{\left(1-i\tau_x\left(L\right)\right)\left(1-i\tau_y\left(L\right)\right)}}\int_0^L\frac{\exp\left(i\Delta kz'\right)}{\sqrt{\left(1-i\tau_x\left(z'\right)\right)\left(1-i\tau_y\left(z'\right)\right)}}$$
$$\times\exp\left(-\frac{2\left(x-(\mathrm{L}-\mathrm{z}')\tan\left(\rho\right)\right)^2}{w_{0,x}^2\left(1-i\tau_x\left(L\right)\right)}-\frac{2y^2}{w_{0,y}^2\left(1-i\tau_y\left(L\right)\right)}-\frac{2\left(1+i\zeta\right)}{\tau^2}\left(\mathrm{t}-\frac{L}{v_g\left(2\omega_0\right)\cos\left(\rho\right)}+GVM\cdot z'\right)^2\right)dz'.$$

(A.4)

Where $GVM = \frac{1}{v_g(2\omega_0)\cos(\rho)} - \frac{1}{v_g(\omega_0)}$ is the group velocity mismatch.

In order to evaluate the efficiency of the SHG process, we start by calculating the pulse energy of the entering pump beam using the envelope in Eq. (A.1):

$$U_p = \frac{1}{2}\varepsilon_0 c n_p \int_{-\infty}^{\infty}\int_{-\infty}^{\infty}\int_{-\infty}^{\infty} \left|E_p(x,y,0,t)\right|^2 dxdydt = \frac{\pi^{3/2}\varepsilon_0 c n_p}{4\sqrt{2}} w_{0,x} w_{0,y} \tau \left|E_0\right|^2. \quad \text{(A.5)}$$

Similarly, the pulse energy of the generated SH field at the output end of the crystal $\mathrm{z = L}$ may be written in a general form using Eq. (A.4) and some algebraic manipulation:

$$U_{sh} = \frac{1}{2}\varepsilon_0 c n_{sh} \int_{-\infty}^{\infty}\int_{-\infty}^{\infty}\int_{-\infty}^{\infty} \left|E_{sh}(x,y,L,t)\right|^2 dxdydt$$

$$= \frac{\pi^{3/2}\varepsilon_0 c n_{sh}}{16}\left|\kappa\right|^2 w_{0,x} w_{0,y} \tau \left|E_0\right|^4 \int_0^L\int_0^L \frac{\exp\left(i\Delta k\left(z_1 - z_2\right)\right)\exp\left(-\frac{\left(z_1 - z_2\right)^2}{L_{s-t}^2}\right) dz_1 dz_2}{\sqrt{\left(1 - i\tau_x(z_1)\right)\left(1 - i\tau_y(z_1)\right)\left(1 + i\tau_x(z_2)\right)\left(1 + i\tau_y(z_2)\right)}}.$$

(A.6)

Defining $L_{s-t} = \left(\frac{\tan^2(\rho)}{w_{0x}^2} + \frac{\zeta^2 + 1}{\tau^2} GVM^2\right)^{-1/2}$ as the effective walk-off length.

Therefore, the general expression for the efficiency of the SHG process is derived by using Eq. (A.5) and (A.6):

$$\eta_{sh} = \frac{U_{sh}}{U_p} = \frac{\gamma U_p}{\sqrt{\pi} w_{0,x} w_{0,y} \tau} \int_0^L\int_0^L \frac{\exp\left(i\Delta k\left(z_1 - z_2\right)\right)\exp\left(-\frac{\left(z_1 - z_2\right)^2}{L_{s-t}^2}\right) dz_1 dz_2}{\sqrt{\left(1 - i\tau_x(z_1)\right)\left(1 - i\tau_y(z_1)\right)\left(1 + i\tau_x(z_2)\right)\left(1 + i\tau_y(z_2)\right)}},$$

(A.7)

where $\gamma = \frac{2n_{sh}|\kappa|^2}{\pi\varepsilon_0 c n_p^2}$.

As mentioned, the walk-off angle in x-ray SHG arises from the noncollinear nature of the phase-matching scheme, as seen in Fig. A.2, as opposed to the Poynting vector walk-off due to the propagation of an extraordinary polarized SH in a birefringent material.

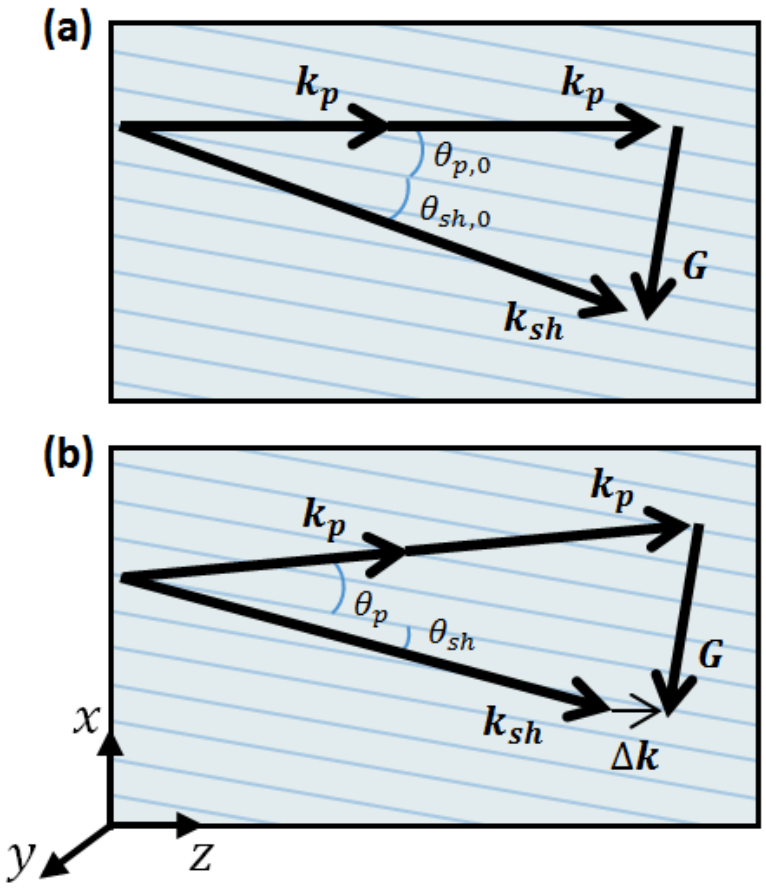

FIG. A.2. *The SHG process phase-matching scheme in the case of (a) perfect phase-matching, and (b) some nonzero phase mismatch.*

Assuming that in perfect phase-matching condition the pump wave-vector $\vec{k}_p$ is parallel to the z direction, as in Fig. A.2(a), and the scattering plane lays in the x-z plane, we decompose the arbitrary phase mismatch vector $\Delta\vec{k} = 2\vec{k}_p + \vec{G} - \vec{k}_{sh}$ into its two components:

$$\Delta k_x = 2k_p \sin\left(\theta_p - \theta_{p,0}\right) - G\cos\left(\theta_{p,0}\right) - k_{sh}\sin\left(\theta_{p,0} + \theta_{sh}\right) \quad \text{(A.8a)}$$

$$\Delta k_z = 2k_p \cos\left(\theta_p - \theta_{p,0}\right) - G\sin\left(\theta_{p,0}\right) - k_{sh}\cos\left(\theta_{p,0} + \theta_{sh}\right) \quad \text{(A.8b)}$$

Where $\theta_{p,0}$ and $\theta_{sh,0}$ are the pump and SH carrier wave-vector angles relative to the atomic planes at perfect phase-matching geometry, respectively, as shown in Fig. A.2.

The integration with respect to z' in Eq. (A.4) displays the fact that the propagation problem of the SHG process is solved by accumulating the contributions to the SH output field generated by infinitesimal slabs at each z' inside the crystal. Therefore, it will be convenient to choose the mismatch vector to be entirely in the z direction $\Delta\vec{k} = \Delta k_z \hat{z}$, having perfect phase-matching in the direction parallel to the crystal surface $\Delta k_x = 0$. In the case of monochromatic plane waves, this restriction on the phase mismatch vector origins from boundary conditions [34].

In the discussion of Chapter 2, a symmetric Laue geometry is assumed, as in Fig. (1.1), where z is directed normal to the crystal surface. In order to use the derivations made in this appendix, we simply replace the crystal length L by $\frac{L}{\cos\left(\theta_p\right)}$, in accordance with the different propagation geometry. Although the

pump and SH waves have changed their propagation direction, in the regime of $L_{s-t} \ll L$, where the contribution of the first and last interaction lengths are negligible relative to the SH signal generated throughout the whole crystal, it is still possible to use Eq. (A.7) and assume a phase mismatch in the form of $\Delta\vec{k} = \Delta k_z \hat{z}$, since the correct boundary conditions $E_{sh}\left(x, y, z = 0, t\right) = 0$ are assumed.

תקציר

ההפעלה המוצלחת של לייזרי אלקטרונים חופשיים, המייצרים פולסי x-ray קצרים ביותר בעלי בהירות גבוהה, מהווה כלי חדש וחשוב למדע העוסק באינטרקציות בין אור לחומר. ה'סינכרוטרונים מדור רביעי' החדשים האלו איפשרו לאחרונה בחינת תהליכים אופטיים לא-לינאריים, תוך כדי הרחבת האופטיקה הלא-לינארית לתחום ה-x-ray. בעבודה זו, אני בוחן תאורטית שני נושאים הנוגעים לאופטיקה לא-לינארית באורכי גל שבתחום הx-ray, תוך כדי התחשבות בהבדלים בין תהליכים אלו לתהליכים בתחום האופטי הנחקר יותר.

הנושא הראשון אותו אני בוחן הינו הכפלת תדר מפולסים קצרים ומפוקסים. גאומטריית התקדמות הגלים בתהליך זה יוצרת שני מאפיינים ייחודיים. ראשית, היא מגבילה את מרחק החפיפה בין הפולס השואב להרמוניה השנייה הנוצרת. שנית, ההרמוניה השנייה הנוצרת מתפזרת חלקית כתוצאה מפיזור בראג. בעבודה זו, אני מתמקד בשימוש בפולסים קצרים ומפוקסים, החיוניים עבור מדידת אפקט לא-לינארי חלש זה. על מנת ללמוד הבטים שונים של תהליך זה ודרכים לייעולו, אני מדמה נומרית ומגיע לביטויים מקורבים עבור היעילות והטולרנטיות של תהליך הכפלת התדר.

הנושא השני בעבודה זו הינו הצגה של שיטה המיועדת לאפיון מבנה השדה הזמני של פולסי x-ray קצרים, כולל מידע על מופע השדה. שיטה זו, המבוססת על גישת אפיון מוצלחת בתחום האופטי, מסתמכת על התאבכות במישור התדר של שני העתקים של הפולס הנבדק, כאשר הם מוסטים בתדר על ידי תהליך לא-לינארי של ערבוב של שלושה גלים עם קרניים בתחום האור הנראה או התת-אדום. בשימוש עם ספקטרומטר המאפשר מדידה של כל רכיבי הספקטרום בו-זמנית, שיטה זו מאפשרת, לראשונה, בחינה של פולסי x-ray בודדים עם משרעת ומופע אקראי. מובאות דוגמאות לאפיון של פולסים אקראיים, ביחד עם אמות מידה למדידה מוצלחת.

עבודה זו נעשתה בהדרכתו של

דר' שרון שוורץ

מן המחלקה לפיזיקה של אוניברסיטת בר אילן

אוניברסיטת בר אילן

הכפלת תדר אופטית ואפיון של פולסים קצרים בתחום קרני ה-X

שמעון יודוביץ'

עבודה זו מוגשת כחלק מהדרישות לשם קבלת תואר מוסמך
במחלקה לפיזיקה של אוניברסיטת בר-אילן

רמת גן תשע"ה